JOURNAL OF GEOPHYSICAL RESEARCH, VOL. 114, B01406, doi:10.1029/2008JB005597, 2009

Direct measurement of strain rates in ductile shear zones: A new method based on syntectonic dikes

C. Sassier,[1,2] P. H. Leloup,[1] D. Rubatto,[3] O. Galland,[4] Y. Yue,[5] and Ding Lin[5]

Received 17 January 2008; revised 31 August 2008; accepted 29 October 2008; published 23 January 2009.

[1] We describe a new method to estimate directly ductile strain rates at an outcrop scale from the deformation of dikes emplaced within a shear zone. The method is tested in a well-constrained shear zone: the Ailao Shan–Red River shear zone, for which global strain rates can be calculated from published fault rates. The strain rate was determined by measuring independently the shear strain (γ) recorded by the dikes and the age (t) of dikes emplacement. The shear strain was quantified by three different methods that take into account either the stretching of the dikes or their angle variations during deformation or both of them. The values of minimum shear strains range between 0.2 and 9.7 for the less to the most deformed dikes, respectively. The ages of dike emplacement were obtained by Th-Pb sensitive high-resolution ion microprobe (SHRIMP) dating of monazites. We obtained three groups of ages: the younger age is 22.55 ± 0.25 Ma, the intermediate age is 26.81 ± 0.66 Ma, and the oldest ages are 29.89 ± 0.46 Ma and 29.93 ± 0.38 Ma. The geochronological data are in agreement with the structural data, the most deformed dikes being the oldest. The minimum strain rates deduced from these measurements are 3 to 4 $\times$ 10^{-14} s^{-1}, which is consistent with previous estimates of geological strain rates in ductile shear zones.

Citation: Sassier, C., P. H. Leloup, D. Rubatto, O. Galland, Y. Yue, and D. Lin (2009), Direct measurement of strain rates in ductile shear zones: A new method based on syntectonic dikes, *J. Geophys. Res.*, *114*, B01406, doi:10.1029/2008JB005597.

1. Introduction

[2] Until recently, the rheological architecture of the continental lithosphere has been matter of intense debates: some studies argue that the lithosphere is strong [e.g., *Tapponnier et al.*, 1982; *Davy and Cobbold*, 1988, 1991; *Handy and Brun*, 2004], whereas others argue that the lithosphere is weak [e.g., *England and McKenzie*, 1982; *Houseman and England*, 1993; *England and Molnar*, 1997; *Copley and McKenzie*, 2007]. The rheology of lithospheric rocks is the first-order parameter that controls their deformation mode. In ductile regime, one might expect that the deformation is distributed when the lithosphere is weak (i.e., Basin and Range province [*Brun*, 1999]), whereas one might expect that the deformation is localized when the lithosphere is rigid (e.g., North Anatolian Fault [*Armijo et al.*, 1999; *Hubert Ferrari et al.*, 2003]). For each mode, the resulting strain rates should be different, i.e., with increasing localization the strain rate increases. Thus, measurement of natural strain rates provides a major constrain on the deformation mode of the crustal rocks, and so on the rheology of the lithosphere.

[3] Although displacement rates in the brittle upper crust are easily measurable from Global Positioning System (GPS), measuring strain rates in the lower ductile crust is a major challenge [*Ramsay*, 2000]. Indeed, ductile deformation of rocks only occurs at high temperature in the deep crust, so that it is impossible to measure in situ the amount and rates of deformation. Thus, strain rates have to be retrieved from exhumed deformed rocks. This is a difficult task because the original shapes and sizes of the deformed geological "objects" are often lost during deformation, particularly after strong deformation that has induced important recrystallization. Another problem in determining deformation rates is the difficulty to precisely date deformation increments.

[4] In order to avoid these difficulties, strain rates are commonly inferred indirectly. Classically, this is achieved by estimating stresses by paleopiezometry, and use the resulting stress values into a quartz flow law [*Hacker et al.*, 1990; *Hacker et al.*, 1992; *Dunlap et al.*, 1997; *Stöckhert et al.*, 1999; *Xypolias and Koukouvelas*, 2001; *Stipp et al.*, 2002; *Gueydan et al.*, 2005]. However, the resulting strain rate estimates strongly depend on (1) the choice of the paleopiezometric law, (2) the choice of the flow law, and (3) the estimate of the deformation temperature. This method provides estimates of local strain rates, but it requires a very precise control of the temperature. A second

[1]Laboratoire des Sciences de la Terre, Université de Lyon, Ecole Normale Supérieure de Lyon, Université Claude Bernard Lyon 1, CNRS, Villeurbanne, France.
[2]Now at Volcanic Basin Petroleum Research, Oslo, Norway.
[3]Research School of Earth Sciences, Australian National University, Canberra, Australia.
[4]Physics of Geological Processes, Universitetet i Oslo, Oslo, Norway.
[5]Institute of Tibetan Plateau Research, Chinese Academy of Sciences, Beijing, China.

0148-0227/09/2008JB005597$09.00

Table 1. Symbols, Parameters and Units Used in This Study

Symbol	Parameter	Unit
e	elongation	
l_f	final length	m
l_i	initial length	m
l_p	length of segment p	m
t	time	s
S	surface of dike	m^2
w_f	final width of dike	m
w_i	initial width of dike	m
w_m	width of largest boudin (D12)	m
w_{sp}	width of the portion	m
w_u	width of the undeformed part of dike D12	m
α_f	final angle of dikes with respect to foliation	
α_i	initial angle of dikes with respect to foliation	
γ	shear strain	
γ_A	shear strain from angle method	
γ_{Ap}	shear strain of the segment p from angle method	
γ_C	shear strain from combined method	
γ_S	stretching shear strain	
ε	quantity of deformation	
$\dot{\varepsilon}$	strain rate	s^{-1}
λ	quadratic extension	
ψ	shearing angle	

possibility is to divide the displacement rate of a shear zone by its width. In this method, the deformation is assumed homogeneous in space and time and depends on the shear zone width. Thus, the estimate of the strain rate only represents an average in space and time for the whole shear zone. A third indirect method was developed for snowball garnets [*Biermeier and Stüwe*, 2003]; the rotation rate of garnet porphyroblasts was deduced by finite element modeling, and the growth rate of the garnet was estimated from the major and trace elements distribution, the grain size distribution and geobarometry. The main assumption in this method is the heating rate on which the estimate of the garnet growth rate is based.

[5] Direct measurement of local strain rates have been achieved so far in only two ways [*Christensen et al.*, 1989; *Müller et al.*, 2000]. Both of them combine a quantification of the deformation recorded by a geological object, and geochronology. The first case is based on helicitic metamorphic garnets that rotated during deformation [*Christensen et al.*, 1989]. The method consists of measuring independently the variations of the rotation angle of the helicitic garnet and the corresponding age using Sr isotopes. The second case refers to the growth of syntectonic fibrous strain fringes during successive deformation phases [*Müller et al.*, 2000]. It consists of estimating the strain recorded by the fringes, and dating them with the Rb-Sr method. These two methods provided values of strain rate in agreement with strain rates reported by *Pfiffner and Ramsay* [1982] in shear zones. However, these methods are very specific and have been rarely applied [*Christensen et al.*, 1994]. In addition, these methods only provide strain rates at a mineral scale, and the extrapolation of these results to large-scale shear zones is disputable. To date, no direct estimate of strain rates at a larger scale (i.e., outcrop) exists.

[6] In this paper, we describe a new method to measure directly local strain rate at the outcrop scale (decameter scale). Our method is based on deformed syntectonic dikes of different generations. It consists of restoring the deformed dikes to quantify the shear strain, and of dating these dikes by Th-Pb analysis of monazite. We have applied our method in a large ductile shear zone: the Ailao Shan–Red River shear zone in SE Asia (ASRRSZ), for which timing and offset are well constrained [e.g., *Briais et al.*, 1993; *Leloup et al.*, 2001b; *Gilley et al.*, 2003]. The ASRR shear zone represents a natural laboratory to measure and test direct measurements of strain rates.

2. A New Method for the Measurement of Strain Rates Within Shear Zones

[7] The strain rate corresponds to the amount of deformation recorded by an object during the time span of deformation, and is summarized by the equation:

$$\dot{\varepsilon} = \frac{\Delta\varepsilon}{\Delta t}. \tag{1}$$

Here $\dot{\varepsilon}$ (s^{-1}) is the strain rate, $\Delta\varepsilon$ (no dimension) is the amount of deformation, and Δt (s) is the time span of deformation. For clarity, we report the definitions of all parameters used in this study in Table 1.

[8] According to equation (1), the strain rate calculation requires both the deformation $\Delta\varepsilon$ and the time interval Δt during which deformation occurred to be constrained. In high-grade shear zones, recrystallization is intense and the initial shapes of the protolith features are commonly lost. In contrast, various objects that formed during deformation (syntectonic) are likely to have accumulated different amounts of deformation and may record different ages. Therefore, syntectonic objects are important objects for estimating local strain rates in high-grade shear zones. Dikes, which are frequently emplaced within shear zones during deformation and can be dated, are good candidates for such a purpose.

2.1. Theoretical Background

2.1.1. Shear Strain Definitions

[9] During deformation within a shear zone, passive markers rotate and change length from l_i to l_f (Figure 1). The change in length can be quantified by the elongation e or by the quadratic extension λ [*Ramsay*, 1967]:

$$e = \frac{l_f - l_i}{l_i}, \tag{2}$$

$$\lambda = (1+e)^2 = \left(\frac{l_f}{l_i}\right)^2. \tag{3}$$

[10] Negative elongation e corresponds to finite shortening and positive ones to finite stretching. Therefore, λ is smaller than 1 for shortening and larger than 1 for stretching. If the deformation regime is close to simple shear, the deformation can be considered in the X-Z plane, and initial (α_i) and final (α_f) orientations of the passive marker can be measured with respect to the shear direction (Figure 1). The

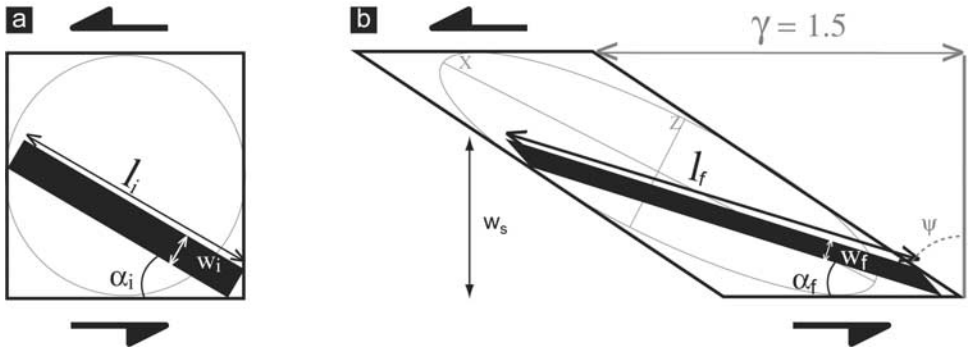

Figure 1. Schematic diagram of simple shear nomenclature. The black rectangle is an object that deforms passively and homogeneously. (a) The object prior to deformation and (b) in a deformed state corresponding to $\gamma = 1.5$. The corresponding strain ellipsoid is represented. View in the X-Z plane.

amount of deformation can then simply be quantified by the shear strain:

$$\gamma = \tan \psi. \tag{4}$$

Here, ψ is the rotation angle of a line originally perpendicular to the shear direction (Figure 1). The quadratic extension λ and final orientation α_f of any passive marker only depend on its original angle α_i and on the shear strain γ (Figure 1) [*Ramsay and Huber*, 1983]:

$$\lambda = -\frac{1}{2}\gamma^2 \cos 2\alpha_i + \gamma \sin 2\alpha_i + \frac{1}{2}\gamma^2 + 1 \tag{5}$$

$$\cot \alpha_f = \gamma + \cot \alpha_i. \tag{6}$$

Combining equations (5) and (6) leads to a direct relationship between λ, α_i, and α_f:

$$\lambda = \left(\cot^2 \alpha_f + \cot^2 \alpha_i - 2 \cot \alpha_f \cot \alpha_i\right) \sin^2 \alpha_i + \left(\cot \alpha_f - \cot \alpha_i\right) \sin 2\alpha_i + 1. \tag{7}$$

Therefore, if the initial orientation (α_i) of the deformed passive marker is known, λ can be calculated by simply measuring the final orientation (α_f) of that marker.

2.1.2. Shear Strain Calculation

[11] When the shear deformation is small, the shape of the deformation ellipsoid can be determined by only measuring λ in various directions for several deformed objects [*Fry*, 1979]. In contrast, when the shear deformation is strong, such a simple analysis is not possible: for shear strains larger than 6, the *x* axis is close to the shear direction and all lines become nearly parallel to each other. However, according to equations (5) and (6), the measurement of λ or α_f in the field and an assumption of α_i may yield the shear strain γ.

[12] According to equation (5), the quadratic extension λ is a function of γ and α_i. Thus, for a given initial orientation α_i, we can plot λ with respect to γ as illustrated in Figure 2a. Therefore, we can estimate γ for any values of λ. Such method, hereafter referred to as the stretching method, was used by *Lacassin et al.* [1993] to estimate shear strains in two major shear zones of SE Asia. Given the shape of the curves, the stretching method is suitable for moderate and high elongation values ($\lambda \geq 5$) and initial angles ($15 \leq \alpha_i \leq 90$, Figure 2a). In contrast, this method is not accurate when λ is small, especially when α_i is small, and is not suitable for very high strains. Notice that if α_i is larger than 90°, a deforming object first shortens, so that λ decreases and is smaller than 1 (Figure 2a); as deformation proceeds, the angle of the object decreases and reaches 90°. Then, the object starts stretching, and λ increases.

[13] According to equation (6), one can simply estimate the shear strain γ if the initial and final angles are known. Hereafter, this method will be called the angle method (Figure 2b). For a given value of α_i, one can plot α_f with respect to γ. Given the shape of the curves, the angle method is accurate only for small deformation and relatively high α_i. For any $\alpha_i \geq 15°$, final angles (α_f) lower than 5° indicate that the shear strains are larger than 8.

[14] Both the stretching and angle methods require an assumption about the initial angle α_i. In the field, the initial shape of passive markers is usually unknown, and so is α_i. To avoid such an assumption, we propose a third method we called the combined method. According to equation (7), for any given values of α_f, one can plot λ with respect to α_i (Figure 2c). Thus, for a deformed object, one can calculate its quadratic extension from equations (2) and (3) and measure its final angle α_f; then a calculated initial angle (α_{ic}) can be estimated (Figure 2). The resulting value of α_{ic} can then be inserted in equation (5) or (6) to calculate γ (Figures 2a and 2b).

[15] In these three methods, the deformation is assumed close to simple shear. In addition, the measured objects must deform and rotate passively in the matrix. In practice, the main difficulties are the estimates of α_i and λ, as well as the precise measurement of α_f for the most deformed objects.

2.2. Dating of Deformation

[16] At the time of their emplacement (crystallization) in an active shear zone, dikes begin to deform. Therefore, dating the emplacement of single dikes puts constraints on the beginning of their deformation. Several dating methods can be used, depending mostly on the temperature conditions at the time of dike emplacement. When deformation occurs at temperature well below the temperature of the intruding magma, cooling will be fast and several methods can yield good results. For example the $^{39}Ar/^{40}Ar$ method

on amphiboles, micas, K-feldspar or whole rock will be suitable for temperatures below 500°C [e.g., *McDougall and Harrison*, 1988]. For higher temperatures, often found in major ductile shear zones, one has to rely on isotopic systems with higher closure temperatures like U-Pb in zircons and monazites. These minerals are robust at high-temperature conditions and their closure temperature for Pb is higher than 700°C [e.g., *Lee et al.*, 1997; *Cherniak and Watson*, 2001; *Cherniak et al.*, 2004]. Zircon often preserves inherited ages even in rocks that underwent partial melting, which may be resolved by using microbeam techniques. Monazite has the advantage of being more reactive to temperature [e.g., *Rubatto et al.*, 2001], often exhibiting little inheritance, and being more radiogenic, thus allowing higher precision at young ages. Nevertheless, excess of ^{206}Pb directly linked to initial disequilibrium in ^{230}Th have been reported in young monazites from leucogranites [*Schärer*, 1984; *Schärer et al.*, 1990]. One way of avoiding this problem is to use the ^{232}Th-^{208}Pb isotopic system [*Harrison et al.*, 1995], which is now considered as the most reliable dating method for young monazites [e.g., *Catlos et al.*, 2004].

[17] Dating the end of deformation is more challenging. Such information usually cannot be obtained for each dike directly. It is however possible indirectly if the deformation ended below a given temperature, and if the cooling history of the dike has been constrained, for example by ^{39}Ar/^{40}Ar and fission track dating [*Leloup et al.*, 2001b]. Another possibility is to use crosscutting relations between deformed and undeformed objects, if undeformed objects can be dated. In this paper, we will use this latter method. Alternatively, plate kinematics can provide good constraints of the timing of the end of deformation.

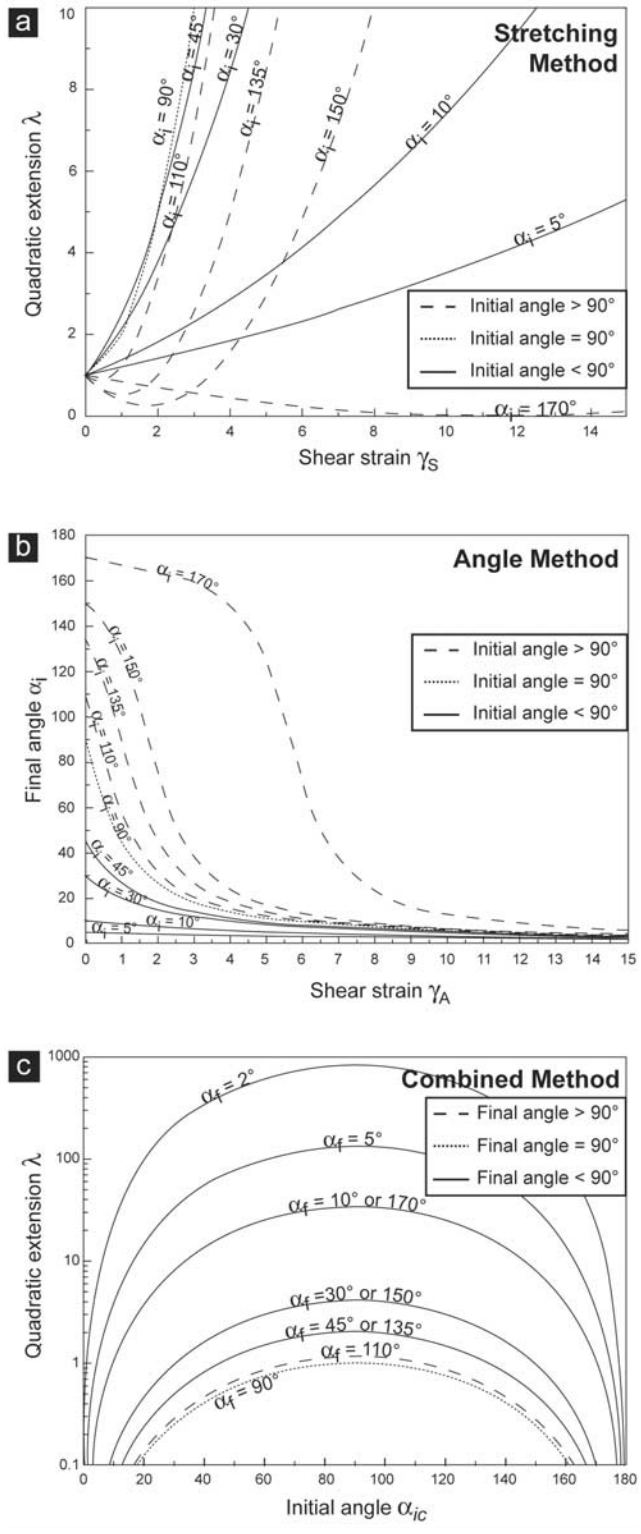

Figure 2. Graphs showing theoretical calculation of shear strains for simple shear with 3 methods described in text. (a) Plots of quadratic extension (λ) versus shear strain (γ), representing stretching restoration method. Curves illustrate equation (5) for different values of initial angles (α_i). Differences are important whether $\alpha_i < 90°$ (full lines), $\alpha_i > 90°$ (dashed lines), and $\alpha_i = 90°$ (dotted line). Shear strains γ are calculated from measured λ and assumed α_i. See text for explanation. (b) Plots of final angles (α_f) versus shear strain (γ), representing angle restoration method. Curves illustrate equation (6) for different values of initial angles (α_i). Legend is similar to that of Figure 2a. Strains γ are calculated from measured α_f and assumed α_i. See text for explanation. (c) Plots of quadratic extension (λ) versus calculated initial angle (α_{ic}). Curves illustrate equation (7) for measured final angles of dikes (α_f); α_{ic} are calculated from measured λ and α_f. Curves are full lines when $\alpha_f < 90°$, dashed lines when $\alpha_f > 90°$, and dotted line for $\alpha_f = 90°$.

3. In Situ Strain Rate Measurements in the Ailao Shan–Red River Shear Zone

3.1. Geological Setting

[18] In continental SE Asia, a major geological discontinuity stretches for more than 1000 km from Tibet to the Tonkin Gulf separating the South China and Indochina blocks [e.g., *Huang*, 1960; *Bureau of Geology and Mineral Resources of Yunnan*, 1983; *Helmcke*, 1985] (Figure 3a). That discontinuity corresponds partly to the active right-lateral Red River Fault Zone (RRFZ) [*Tapponnier and Molnar*, 1977; *Allen et al.*, 1984; *Leloup et al.*, 1995; *Wang et al.*, 1998a; *Replumaz et al.*, 2001; *Schoenbohm et al.*, 2006]. Four narrow (10–20 km wide) high-grade metamorphic ranges (XueLong Shan, XLS; Diancang Shan, DCS;

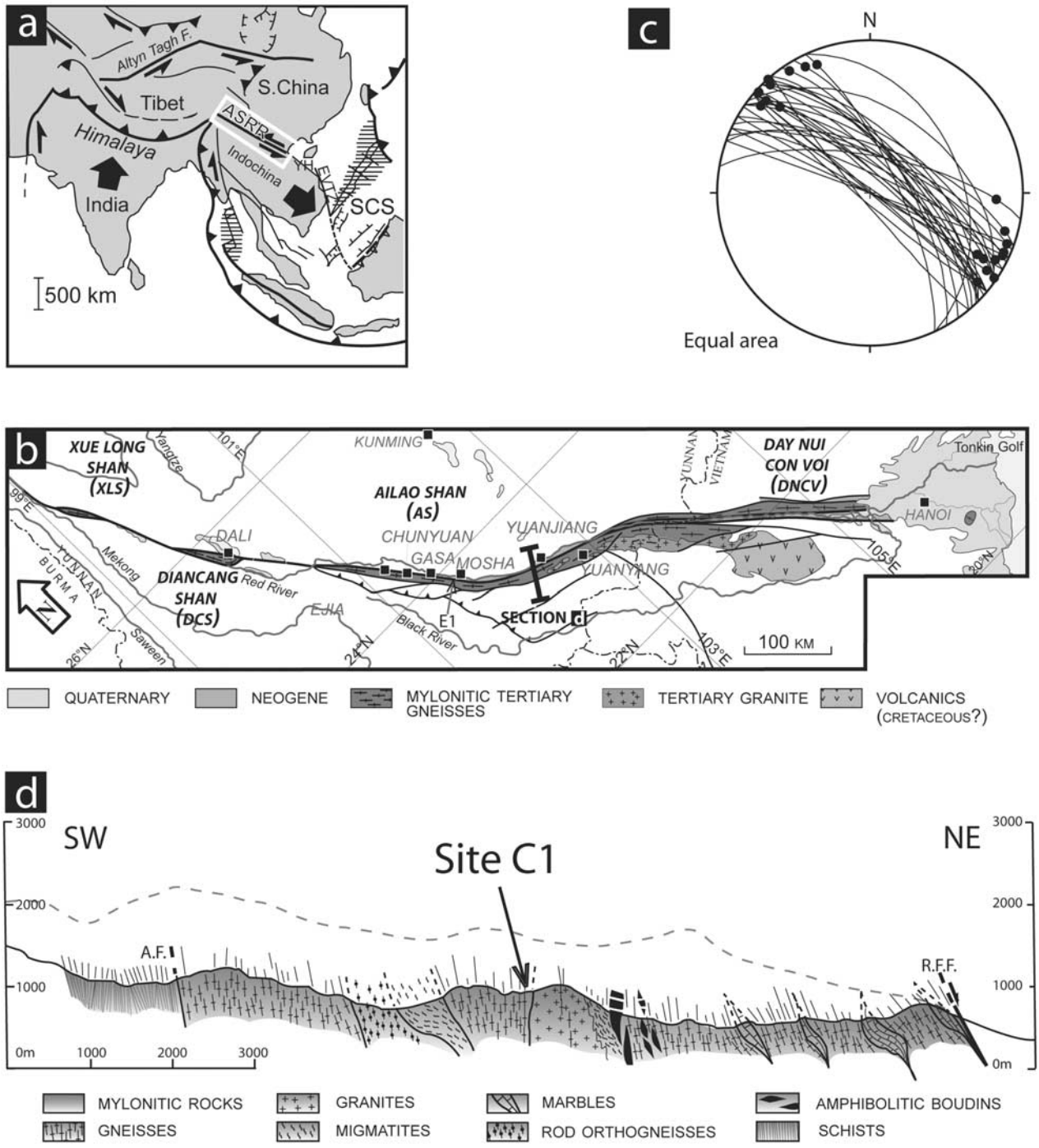

Figure 3. Geological map of Ailao Shan–Red River shear zone (ASRRSZ). (a) Location of ASRRSZ in India-Eurasia collision setting. ASRR, Ailao Shan–Red River, SCS, South China Sea, YH, Yingehai basin, EVTZ, East Vietnam transform zone. (b) Simplified map of ASRR shear zone. Modified after *Leloup et al.* [2001b]. (c) Stereographic projection (Schmidt diagram, lower hemisphere) of foliations (great circles) and lineations (dots) in gneisses along YuangJiang cross section of ASRRSZ. Modified after *Leloup et al.* [1995] with permission from Elsevier. (d) YuangJiang geological cross section of Ailao Shan metamorphic range. Modified after *Leloup et al.* [1995] with permission from Elsevier. Section locates site C1 (see Figure 4).

Ailao Shan, AS; and Day Nui Con Voi, DNCV, Figure 3b) stretch along the RRFZ. These massifs were initially interpreted as exhumed Precambrian basement thrusted upon Indochina prior to the Triassic [*Bureau of Geology and Mineral Resources of Yunnan*, 1983; *Helmcke*, 1985], but the following studies interpreted them as resulting from exhumation of a large Oligo-Miocene left-lateral shear zone: the Ailao San–Red River (ASRRSZ) [*Tapponnier et al.*,

1986; *Tapponnier et al.*, 1990; *Leloup et al.*, 1993, 1995, 2001b].

[19] Along the ASRRSZ, the metamorphic rocks show intense ductile deformation with a generally steep foliation that bears a horizontal lineation, both being parallel to the trend of the gneisses cores (Figures 3c and 3d). Numerous shear criteria indicate that the gneisses have undergone intense left-lateral shear [*Tapponnier et al.*, 1986, 1990; *Leloup et al.*, 1993, 1995; *Jolivet et al.*, 2001; *Leloup et al.*, 2001b; *Anczkiewicz et al.*, 2007]. *Leloup et al.* [1995] calculated a total left-lateral offset of 700 ± 200 km from six different types of geological formations. These values were considered as not adequately documented by some authors [e.g., *Wang and Burchfiel*, 1997; *Searle*, 2006].

[20] The DNCV, southernmost range of the ASRR (Figure 3b), exhibits a half-pipe-like structure with stretching lineations constantly parallel to the belt, flat lying high-temperature foliation in the core, and steeper flanks showing both left-lateral shear indicators [*Leloup et al.*, 1995; *Jolivet et al.*, 2001; *Leloup et al.*, 2001b; *Anczkiewicz et al.*, 2007]. *Leloup et al.* [1995, 2001b] interpreted this geometry as resulting from large-scale left-lateral shear and upward thinning of the shear zone in a way comparable to what is observed much farther north in the DCS [*Leloup et al.*, 1993]. However, *Jolivet et al.* [2001] and *Anczkiewicz et al.* [2007] suggested that the high-temperature metamorphism predates the left-lateral shear and argued for a transtensional origin of the DNCV. Furthermore, for *Jolivet et al.* [2001], the central part of the DNCV corresponds to a passively uplifted flat décollement level. In any case, left-lateral transtensional deformation and cooling of the DNCV occurred between ~27 and ~22 Ma [*Nam et al.*, 1998; *Wang et al.*, 1998b, 2000; *Leloup et al.*, 2001b, 2001a; *Anczkiewicz et al.*, 2007]. In the AS massif, rapid cooling occurred diachronously along strike from ~25 Ma in the SE to ~17 Ma in the NW [*Harrison et al.*, 1996]. Such a cooling pattern was interpreted by a "zipper" tectonic model where transtensional deformation lifted up the southeast section of the shear zone [*Harrison et al.*, 1996; *Leloup et al.*, 2001b]. This model yields a quantitative estimate of a left-lateral offset ≥400 km and a fault rate of ~4.8 cm a^{-1} between ~25 and ~17 Ma [e.g., *Leloup et al.*, 2001b]. This model was contested by *Schoenbohm et al.* [2004], who proposed instead a transpressional origin to the exhumation of the ASRR based on the observation of thrusts of possible Miocene age along the northern edge of the AS. However, these thrusts could have formed during N–S compression after the end of the left-lateral shear.

[21] Petrologic studies showed that strain occurred under a high geothermic gradient, from a metamorphic peak in amphibolite facies conditions at 4.5–8 kbar/700°C in the Ailao Shan [*Leloup and Kienast*, 1993] and ~6.5 kbar/≥700°C in the Day Nui Con Voi [*Nam et al.*, 1998; *Leloup et al.*, 2001b]. In these massifs, left-lateral deformation pursued in greenschist facies conditions (<4 kbar/~500°C) [*Leloup and Kienast*, 1993; *Nam et al.*, 1998; *Jolivet et al.*, 2001; *Leloup et al.*, 2001b]. In the AS and DCS massifs, the high-temperature deformation was documented as coeval with felsic and alkaline magmatism dated from 35 to 22 Ma [*Schärer et al.*, 1994; *Zhang and Schärer*, 1999]. Moreover, monazite dating from the mylonitic fabric and synkinematic garnets constrained the duration of high-temperature metamorphism from 34 to 21 Ma in the XLS, DCS, AS, and DNCV, while inherited upper Tertiary to Triassic ages are also found in the DNCV [*Gilley et al.*, 2003]. Because left-lateral shear was coeval with cooling, $^{40}Ar/^{39}Ar$ data documented a timing of ductile deformation between ~31 and 17 Ma [*Harrison et al.*, 1992; *Leloup and Kienast*, 1993; *Harrison et al.*, 1996; *Nam et al.*, 1998; *Wang et al.*, 1998b, 2000; *Jolivet et al.*, 2001; *Leloup et al.*, 2001b, 2001a; *Maluski et al.*, 2001; *Garnier et al.*, 2002; *Leloup et al.*, 2007], whereas *Searle* [2006] proposed that left-lateral shear started only after 21 Ma by considering that all deformed granites were prekinematic. From offshore seismic data, *Clift and Sun* [2006] proposed that the Yingehai (YH) basin, lying in the direct prolongation of the ASRRSZ, formed as a left-lateral pull-apart mostly from ~34 Ma until prior to ~14 Ma.

[22] Another point of debate about this area is the possible link between the opening of the South China Sea (SCS) and the kinematics of the ASRRSZ. Different models were proposed: some authors proposed that the opening of the SCS, located at the tip of the ASRRSZ, would result from the accommodation of the relative motion between the laterally extruding Indochina block and South China [*Tapponnier et al.*, 1986; *Briais et al.*, 1993; *Replumaz et al.*, 2001; *Replumaz and Tapponnier*, 2003]. Matching of the magnetic anomalies yields finite and incremental Euler rotation poles describing the relative motion between the SCS margins [*Briais et al.*, 1993]. Assuming that the southern margin was rigidly linked with Indochina, these poles imply ≈540 km of left-lateral strike-slip deformation along the ASRR shear zone between ≈30 Ma and ≈16 Ma with a transpression component in the NW and a transtension component in the SE [*Briais et al.*, 1993]. These values match, both qualitatively and quantitatively, with the onshore data, and with the zipper model, apparently confirming the intimate link between the ASRR and the SCS [e.g., *Briais et al.*, 1993; *Leloup et al.*, 2001b; *Gilley et al.*, 2003].

[23] Other authors have refuted the pull-apart origin of the SCS and proposed instead that a proto-South China Sea would have dragged the south margin of the SCS while subducting below Northwest Borneo [*Holloway*, 1982; *Taylor and Hayes*, 1983; *Hall*, 2002; *Morley*, 2002; *Schellart and Lister*, 2005; *Clift et al.*, 2008]. In this model, ~1400 km of the oceanic crust would have subducted beneath Borneo, drifted along the Luppar line [*Clift et al.*, 2008], and the ASRR left-lateral offset would have died out north of, or within, the YH basin [*Rangin et al.*, 1995; *Wang and Burchfiel*, 1997; *Morley*, 2002, 2007; *Clift et al.*, 2008]. *Clift et al.* [2008] proposed a left-lateral offset ranging between 100 and 280 km on the ASRR based on the assumption of a 1400–1200 km wide proto-SCS. One major problem with that interpretation is that seismic tomography do not image any clear large-scale slab subducting southward below Borneo [*Rangin et al.*, 1999]. Some authors have also argued that NNW–SSE extension in the South China margin started in the Cretaceous/Eocene [*Zhou et al.*, 1995], much earlier than strike-slip motion, suggesting a minor link between the ASRR and the SCS. All these authors suggested that the rollback of the Pacific and/or Sunda subducting slabs was the main driving force

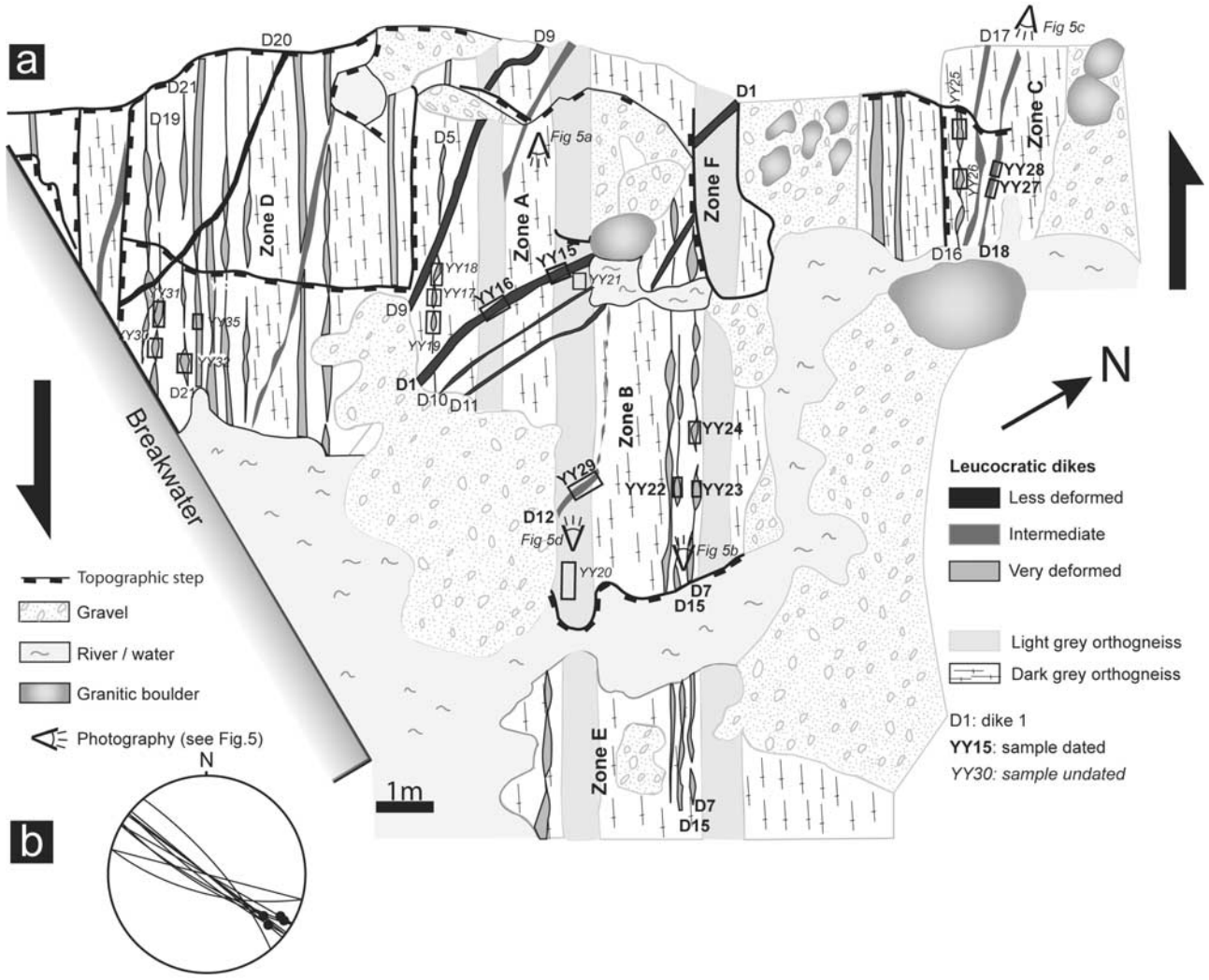

Figure 4. Schematic drawing of studied outcrop (site C1, location on Figure 3). (a) Drawing of view from above of outcrop C1. Drawing shows various deformed leucocratic dikes into orthogneiss host rock. Figure locates studied dikes (D-), sampling sites (YY-), and photographs of Figure 5. (b) Stereographic projections (Schmidt diagram, lower hemisphere) of foliation (great circles) and lineation (arrows) at site C1.

for marginal basin opening [e.g., *Morley*, 2002; *Schellart and Lister*, 2005].

[24] As highlighted in the previous paragraphs, the kinematic and the timing of deformation along the ASRRSZ are largely debated in the literature. The purpose of this paper is not to contribute in this debate, so that we will not discuss it any longer.

[25] Four independent estimates of the timing and fault rate of the ASRR can be proposed from the data summarized above. First, taking the total left-lateral offset from geological markers of 700 ± 200 km and considering that the activity of the shear zone occurred between 34 to 17 Ma [*Leloup et al.*, 2001b] yields an average fault rate of 4.1 ± 1.2 cm a^{-1}. A second estimate is given by the zipper model that suggests a strike-slip fault rate of ~4.8 cm a^{-1} between 25 and 17 Ma. If the correlation in timing and amount of deformation between major sinistral motion on the ASRRSZ and seafloor spreading in the SCS is valid, a third estimate is given by the seafloor spreading rotation poles: 3.7 cm a^{-1} on average [e.g., *Briais et al.*, 1993; *Harrison et al.*, 1996]. These three estimates obtained through independent data sets are close to each other, yielding fault rates (F) between 2.9 and 5.3 cm a^{-1} along the ASRR (4.2 cm a^{-1} on average). A fourth estimate gives lower fault rates between 5 and 11 mm a^{-1} from minimum offsets of 100 to 280 km on the ASRRSZ between ~34 and ~14 Ma [*Clift et al.*, 2008].

[26] The fault rate estimates along the ASRR provide first-order estimates of the strain rate by assuming that all the deformation was accommodated homogeneously within a shear zone of a given width. Given that the metamorphic ranges of the ASRRSZ are 10 to 20 km wide the calculations yields strain rates of 1.3×10^{-13} to 5.9×10^{-14} s^{-1} on average (Table 5). The fact that the strain rates are constrained by three independent sets of observation makes the ASRR a good place to test the measurement method proposed in this paper.

[27] In the Ailao Shan massif, synkinematic leucocratic dikes and amphibolitic levels are common [e.g., *Leloup et*

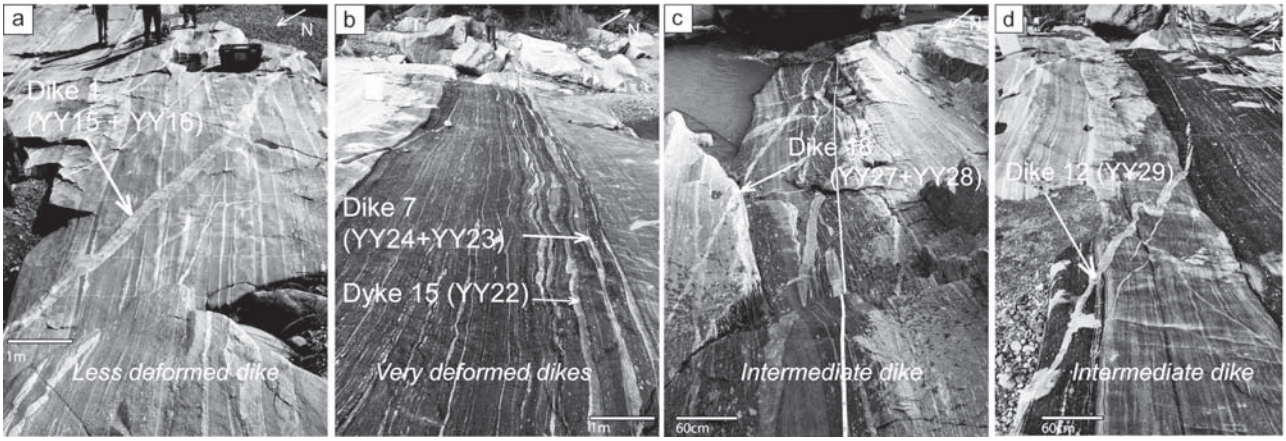

Figure 5. Photographs of sampled syntectonic leucocratic dikes (location on Figure 4). (a) Example of poorly deformed dike (D1, samples YY15 and YY16) crosscutting mylonitic foliation in orthogneiss. (b) Example of very deformed dikes (D7, samples YY24 and YY25 and D15, sample YY22) transposed in foliation and boudinated. (c) Example of dike with intermediate deformation (D18, samples YY27 and YY28), crosscutting mylonitic foliation. (d) Another example of dike with intermediate deformation (D12, sample YY29).

al., 1995]. These dikes are stretched together with the surrounding mylonites. Both the dikes and amphibolitic levels within their gneissic country rock form spectacular boudins trails that have been used to estimate shear strains [*Lacassin et al.*, 1993]. The results of *Lacassin et al.* [1993] show high shear strain in the amphibolites ($\gamma = 33 \pm 6$) and lower ones for the leucocratic dikes ($\gamma = 8 \pm 2$). In order to constrain the age of the high-temperature shearing, some of the largest, and thus probably among the less deformed dikes, have been dated between 22.4 ± 0.2 Ma and 24.1 ± 0.2 Ma using conventional U-Pb dating of monazite, titanite and xenotime [*Schärer et al.*, 1990, 1994]. In most outcrops, deformation is strong enough so that all dikes are transposed parallel to the main foliation, and the end of ductile deformation is difficult to date. However, 3 km SW of YuangJiang, in the orthogneissic core of the Ailao Shan, a large outcrop (Figure 3d, site C1 described by *Leloup et al.* [1995]) exhibits various syntectonic dikes, where the less deformed systematically crosscut the more deformed. This outcrop provides a very good opportunity to quantify the strain rate.

3.2. The Yuang Jiang River Bed Outcrop (Site C1)

[28] The site C1 consists of a large (~50 × 20 m, Figure 4) almost horizontal, water-polished outcrop. It exhibits dark gray orthogneiss, with lighter gray levels, intruded by several leucocratic dikes (Figure 4a). Foliation is well defined by the orientation of micas in the orthogneiss. It is close to vertical and strikes N120° on average (Figure 4b). Stretching lineation, when visible, is nearly horizontal with pitches between 10 and 30° (Figure 4b). The almost horizontal outcrop surface is thus close to the X-Z plane of deformation (perpendicular to foliation and parallel to lineation). Numerous shear criteria within the orthogneiss indicate left-lateral shearing [*Tapponnier et al.*, 1990; *Leloup and Kienast*, 1993; *Leloup et al.*, 1995]. Such a structure is similar to what has been described along the YuanJiang section, and in the whole Ailao Shan range, as a result of intense left-lateral shearing. Deformation close to simple shear has been strong enough so that the maximum flattening plane (X-Y) is almost parallel to the shear plane [e.g., *Leloup et al.*, 1995].

[29] Several generations of variously deformed leucocratic dikes are visible. The less deformed dikes systematically crosscut the most deformed ones. Of the two dozens of syntectonic dikes identified in site C1, five were selected in this study (D1, D12, D18, D7 and D15, Figure 5). They exhibit various amounts of deformation and they are big enough to be sampled for dating. The dike D1 is an almost undeformed dike (like D10 and D11, Figures 4 and 5a) because (1) it cuts the main foliation at high angle (~30°), (2) it is not cut by any shear planes, and (3) it suffered little stretching. Limited necking is visible in three places along D1 (Figure 5a). In contrast, D7 and D15 are highly deformed dikes because they are transposed in the main foliation and now form boudin trails (like D19, D5, and D16, Figures 4 and 5b). The boudins forming D15 are well individualized whereas those of D7 exhibit pinch-and-swell structures. D18 and D12 strike between N150 and N120 and exhibit intermediate strains between the most deformed and the less deformed dikes (Figures 4, 5c and 5d). D12 has a peculiar shape: it shows a nearly undeformed part (part a) comparable to D1, while the other part (part b) is almost transposed in the foliation and forms a boudins trail comparable to D18 and D15 (Figures 4 and 5d).

[30] The simplest interpretation of these patterns is that the dikes intruded continuously during left-lateral shear, the most deformed dikes intruding early in the deformation history, and the less deformed dikes emplacing just prior to the end of that deformation. According to equation (1), such dikes are suitable for strain rate calculations.

3.3. Shear Strain Calculations

3.3.1. Stretching Method

[31] As described in section 2.1.2, the stretching method consists of the measurement of dikes elongations (e) and quadratic extension (λ). Measurement of λ was achieved by boudins trail surface balanced restoration [*Lacassin et al.*,

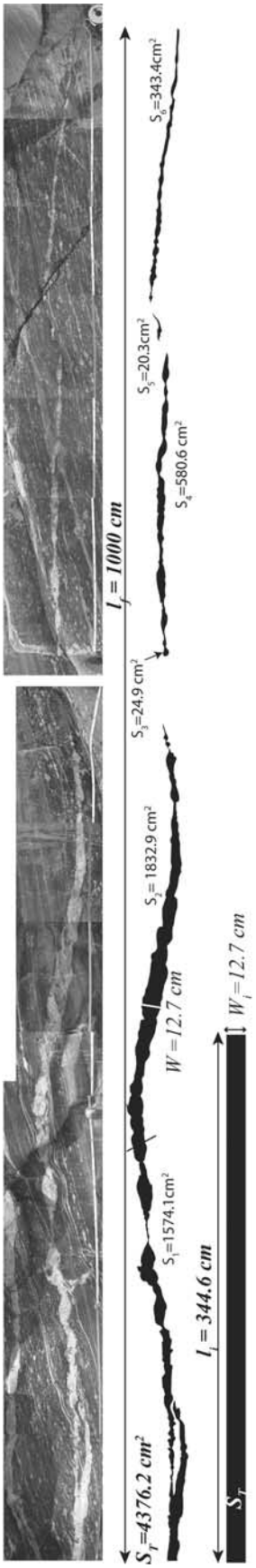

Figure 6. Restoration of boudinaged dike D18 from field photographs (method of *Lacassin et al.* [1993]). Final length (l_f) is measured from decameter ribbon. Boudins surfaces (S_1, S_2, . . .) and maximum width (W) are measured from outline of dike. Total surface (S_T) is sum of all boudins surfaces. Initial width (W_i) is assumed equal to maximum boudin width (W). Method assumes that dike surface is constant during deformation and that initial dike is rectangle of width W_i and of length $l_i = S_T/W_i$.

Table 2. Shear Strain Calculations From Length and Surface Measurements and e, λ, and γ Calculations[a]

		Measured				Calculated			Methods: Stretching	Methods: Angle	Methods: Combined	
Name	Sample	Surface (cm^2)	l_f (cm)	w_i (cm)	Weighed Average α_f	l_i (cm)	e	l	γ_s ($\alpha_i = 30°$)	γ_A ($\alpha_i = 30°$)	Calculated α_{ic} (<90°)	γ_c (α_{ic})
Less deformed dike 1	YY15	17201.2	864	22	26°	781.9	0.11	1.2	0.2	**0.3**	28.5°	**0.2**
Error +4%		*17889.2*				*813.1*	*0.06*	*1.1*	*0.1*			*0.1*
Error −4%		*16513.2*				*750.6*	*0.15*	*1.3*	*0.3*			*0.3*
Intermediate dike 18	YY27	4376.2	1000	12.7	18°	344.6	1.9	8.4	**4**	**1.4**	64	**2.6**
Error +10%		*4813.8*				*379*	*1.64*	*7*	*3.4*			*2.3*
Error −14%		*3763.5*				*296.3*	*2.37*	*11.4*	*4.9*			*3.1*
Dike 12, whole dike	YY29	2815.2	995	9.2	13.9°	306	2.25	10.6	**4.7**	2.3	51.5°	**3.2**
Error +5%	wi = wu	*2956*				*321.3*	*2.1*	*9.6*	*4.4*			*3.1*
Error −4.5%		*2688.5*				*292.2*	*2.4*	*11.6*	*5*			*3.3*
Dike 12, most deformed part b of dike	wi = wm	1057.9	695	**5.2**	8.6°	203.4	2.42	11.7	5	4.9	30.8°	4.9
Error +5%		*1110.8*				*213.6*	*2.25*	*10.6*	*4.7*			*4.8*
Error −4.5%		*1010.3*				*194.3*	*2.58*	*12.8*	*5.4*			*5.1*
	wi = wu	(1057.9)	(695)	**(9.2)**	(8.6°)	(115)	(5.04)	(36.5)	(10.3)	(4.9)	(64.5°)	(6.1)
Error +5%		(*1110.8*)				(*120.7*)	(*4.76*)	(*33.1*)	(*9.7*)			*6*
Error −4.5%		(*1010.3*)				(*109.8*)	(*5.33*)	(*40.1*)	(*10.9*)			*6.3*
Dike 7	YY24	3595.3	1190	7.2	≤5°	499.3	1.38	5.7	**2.9**	≥ 9.7	12°	**6.7**
Error +4%		*3739.1*				*519.3*	*1.29*	*5.3*	*2.7*			*6.3*
Error −5%		*3415.5*				*474.4*	*1.51*	*6.3*	*3.2*			*7.3*
Dike 15	YY22	5118.4	1253	15.6	≤5°	328.1	2.82	14.6	**5.8**	≥ 9.7	19.5°	**8.6**
Error +8%		*5527.9*				*354.4*	*2.54*	*12.5*	*5.3*			*7.9*
Error −14%		*4401.8*				*282.2*	*3.44*	*19.7*	*7.1*			*10.7*
Dike Measurements on the Same Outcrop From Lacassin et al. [1993] *(Recalculated)*												
Boudins D	1		**160**	**1.1**		**26.1**	**5.13**	**37.6**	**10.5**			
	2		**299.5**	**5**	≤5°	**67.2**	**3.46**	**20**	**7.2**	≥ 9.7	23°	**9.1**
Boudins E	1		**114.7**	**4.4**	≤5°	**15.1**	**6.6**	**57.7**	**13.4**	≥ 9.7	41.5°	**10.3**
			(114.7)	(5	(≤5°)	(13.3)	(7.62)	(74.4)	(15.5)	(≥ 9.7)	(49°)	(10.5)
			(114.7)	(3.9)	(≤5°)	(17)	(5.75)	(45.5)	(11.7)	(≥ 9.7)	(36°)	(10.1)
	2		**130.3**	**3.8**	≤5°	**24.2**	**4.38**	**29**	**9**	≥ 9.7	28°	**9.6**
			(130.3)	(2.7)	(≤5°)	(34)	(2.83)	(14.7)	(5.9)	(≥ 9.7)	(19.5°)	(8.6)
	3		**123.9**	**2.7**	≤5°	**33.7**	**2.68**	**13.5**	**5.5**	≥ 9.7	18.5°	**8.6**

[a]Dikes surfaces, final length (l_f), width of the thickest boudin (w), and final angle with respect to the shear direction (α_f) are measured in the X-Z (horizontal) plane from scaled field photographs. Dikes initial restored length (l_i), elongation (e), and quadratic extension (λ) are calculated using the method of *Lacassin et al.* [1993] (Figure 6). Shear strains γ_S, γ_A, γ_C are calculated using the stretching (Figure 7a), angle (Figure 7b) and combined (Figure 7d) methods, respectively. Italics indicate results taking into account uncertainties resulting from the optical deformation of the pictures. Bold indicates most reliable results; values in parentheses indicate alternative results corresponding to alternative initial thicknesses (for certain samples). See text for details.

1993]. As dikes rotated from α_i to α_f and stretched from l_i to l_f during deformation, they correlatively thinned from w_i to w_f (Figure 1). If this thinning was perfectly homogeneous, it would be impossible to estimate the original width w_i. However, the dikes underwent inhomogeneous stretching by boudinage [e.g., *Ramsay*, 1967]. This deformation process locally preserves the original width of the dike, whereas other portions are strongly stretched, even to zero width. By measuring the total length of a boudins trail (l_f) it is possible to calculate its original length (l_i) assuming that the total surface of the dike has been conserved and that the original width of the dike (w_i) is equal to that of the wider boudin (w_m)[*Lacassin et al.*, 1993]. This last assumption probably tends to underestimate e, and thus λ, as homogeneous stretching is neglected.

[32] The outline of boudins trails on scaled pictures provides the final length (l_f), surface (S) and width of each boudin (Figure 6 and Table 2). Errors due to optical deformation of the pictures (italic numbers in Table 2) were calculated from measurement of the deformation of a ribbon decameter. For each dike, the width of the wider boudin w_m of the trail is considered to be the closest estimate of w_i (Table 2). For D12, w_i was also estimated from the width of the less deformed part of the dike (part a), reported as w_u in Table 2. Table 2 gives the corresponding l_i, e and λ for each dike. The values of e range from 0.11 to 2.82, and the corresponding λ range between 1.2 and 14.6. The values obtained from the same outcrop by *Lacassin et al.* [1993] were often higher, ranging from 2.68 to 7.62 for e and from 13.5 to 74.4 for λ (Table 2). Indeed, *Lacassin et al.* [1993] quantified the finite deformation and thus focused on the most deformed dikes while we selected dikes that exhibit boudins large enough to provide suitable samples for dating.

[33] An important observation is that none of the dikes are folded (Figure 5) [*Lacassin et al.*, 1993]. The only deflection that could be interpreted as a fold on D12 (Figure 5d) is not actually a fold since it cuts through a perfectly unfolded foliation. That observation implies all the dikes were emplaced with α_i smaller than 90°. Otherwise, the dikes would have undergone shortening prior to stretching, and consequently folding. Another observation is that the less deformed dikes show an angle close to 30° with respect to the main foliation (D9, D1, D10, D11; Figure 5a). Thus, we chose $\alpha_i = 30°$ to calculate γ (γ_S, Table 2). The resulting γ_S is 0.2 ± 0.1 for D1, $2.9^{+0.3}_{-0.2}$ for D7 and $5.8^{+1.3}_{-0.5}$ for D15 (Figure 7a). Intermediate dikes provide γ_S of $4^{+0.9}_{-0.6}$ and 4.7 ± 0.3 for D18 and D12 respectively (Figure 7a). Additionally, we estimated γ_S for the most deformed part of D12 (part b)

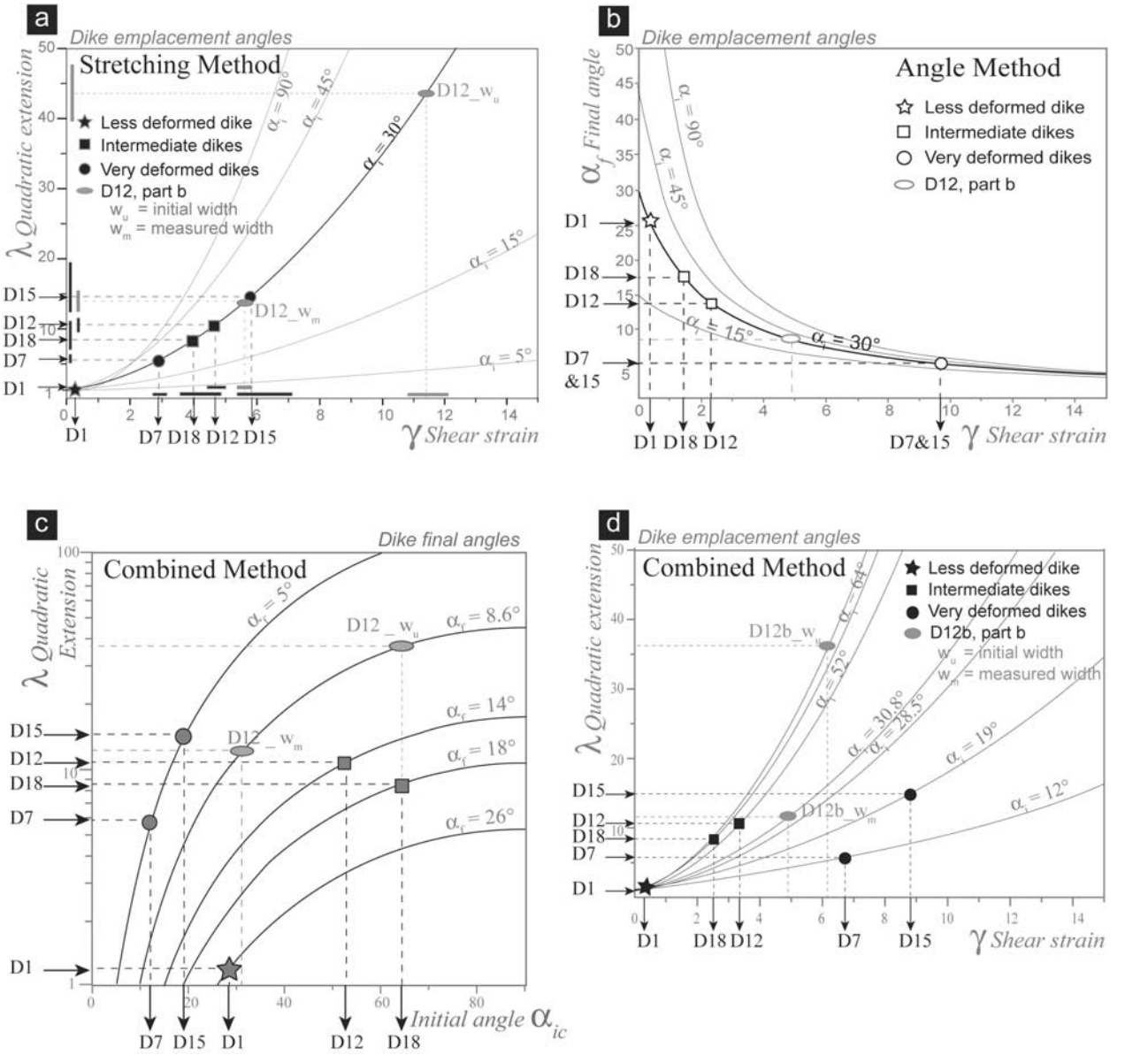

Figure 7. Graphs showing calculation of shear strains for simple shear according to three methods described in text. For explanation, see Figure 2. (a) Plots of quadratic extension (λ) versus shear strain (γ), representing stretching restoration method. In this study, α_i is assumed to be 30°. Points represent studied dikes. See text for details. (b) Plots of final angles (α_f) versus shear strain, representing angle restoration method. Again, α_i is assumed to be 30°. Points represent studied dikes. See text for details. (c) Plots of quadratic extension (λ) versus calculated initial angle (α_{ic}). Each curve corresponds to single value of α_f from each studied dike. Dikes analysis gives λ and α_f, and α_{ic} is calculated. (d) Plots of quadratic extension (λ) versus shear strain (γ). Curves illustrate equation (5) for values of calculated initial angles (α_{ic}) from Figure 7c. Shear strains are calculated from measured λ and calculated α_{ic}. Figures 7c and 7d represent two stages of combined method. See text for details. Table 2 synthesizes all corresponding results.

in order to quantify how much λ was underestimated, when assuming the initial width w_i (see section 4.1). If the width of the wider boudin of part b is taken as initial width, namely $w_i = w_m$, the resulting γ_S is $5^{+0.4}_{-0.3}$. But if the width of the undeformed part of D12 (part a) is taken as the initial width namely $w_i = w_u$, then γ_S is 10.3 ± 0.6. As noticed above and discussed by *Lacassin et al.* [1993], this method probably provides underestimated values of γ_S, mostly because homogeneous deformation is neglected. This is obvious for D7 because it yields a much smaller λ value than D15, which lies parallel to it and has the same age (see below). According to our results, γ_S ranges from 0.2 to 5.8. In contrast, *Lacassin et al.* [1993] measured higher shear strains (recalculated for α_i = 30°) between 5.5 and 15.5; indeed, they analyzed the most deformed dikes only (Table 2), which were too deformed, i.e., too small, to be sampled for dating. This implies we did not analyze the most deformed dikes, i.e., the oldest.

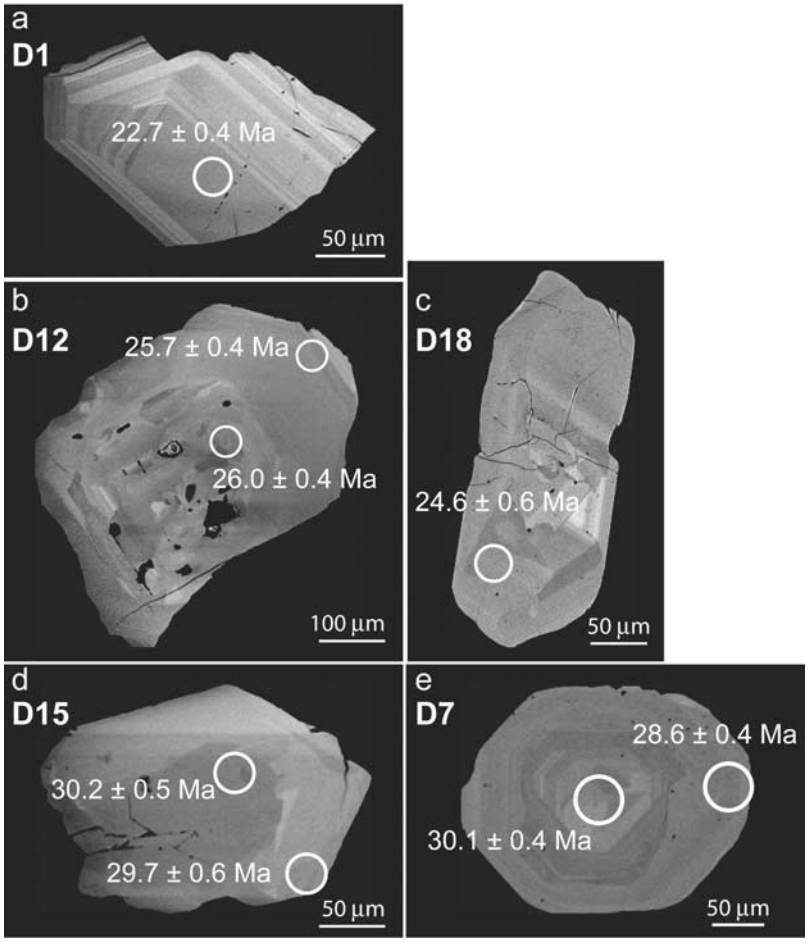

Figure 8. BSE images of monazite grains showing types of zonations. Circles indicate SHRIMP analysis pits for which age ($^{232}Th/^{208}Pb \pm 1$ sigma) is reported. (a) Monazites with magmatic oscillatory zoning from dike D1. (b) Monazites with patchy zoning from dike D12 (intermediate deformation). (c) Monazites with a core rims structure from dike D18 (intermediate deformation). (d) Monazites with planar zoning from strongly deformed dike D15. (e) Monazites with concentric zoning from strongly deformed dike D7.

3.3.2. Angle Method

[34] With the angle method, the estimate of γ (γ_A, Table 2) only depends on the initial (α_i) and final (α_f) angles between the dike and the shear plane (Figure 7b, equation 5). As previously discussed, α_i is assumed to be 30° and α_f was directly measured in the field. However, the dikes are not perfectly linear and α_f varies in different portions of the dike, even if the deformation seems relatively homogeneous (Figure 5). Such geometry could be linked to irregular emplacement or/and to inhomogeneous deformation. Thus, to obtain the best estimate of the general trend of α_f for each dike, we split them in n linear segments of constant angles. For each segment p, the final angle α_{fp} and the length l_p (Figure 1, $l_p = l_f$) were measured. Then, the total final angle (α_{fTotal}) was calculated using the following equation:

$$\alpha_{fTotal} = \operatorname{atan}\left(\frac{\sum_{p=1}^{n} l_p \times \sin\alpha_{fp}}{\sum_{p=1}^{n} l_p \times \cos\alpha_{fp}}\right). \quad (8)$$

[35] According to equation (6), the γ_{ATotal} can be calculated from α_{fTotal} and α_i. Thus combining equations (6) and (8) yields an expression of γ_{ATotal} as a function of the different α_f of the segments of the dikes:

$$\gamma_{Atotal} = \frac{1}{\sum_{p=1}^{n} l_p \sin\alpha_{fp}}\left(\sum_{p=1}^{n} \gamma_{Ap} l_p \sin\alpha_{fp}\right). \quad (9)$$

[36] D1 has a α_{fTotal} of 26° corresponding to a $\gamma_A = 0.3$ that is coherent with result from the stretching method (γ_S, Table 2 and Figure 7b). For D15 and D7, α_f is too small to be accurately measured. It is estimated to be 5° at maximum, giving a minimum value of γ_A at 9.7. These minimum estimates are however much larger than the corresponding γ_S equal to 2.9 for D7 and 5.8 for D15 (Table 2). This confirms again that the stretching method underestimates e and λ when the deformation is strong. In contrast, intermediate dikes D18 and D12 exhibit values of γ_A of 1.4 and 2.3, respectively, which are much lower than their corresponding γ_S of 4 and 4.7 (Table 2). For the dike D12, we also applied the angle method to the very deformed part

(part b), which gives a γ_A of 4.9 (Table 2). Most boudins measured by *Lacassin et al.* [1993] are nearly transposed in the foliation and yield $\gamma_A \geq 9.7$.

3.3.3. Combined Method

[37] Discrepancies between the stretching and the angle methods emphasize inconsistencies between measured λ or e, α_i, and α_f for a given dike. This may mainly arise from underestimates of e because homogeneous deformation is neglected and wrong assumptions on α_ι are taken. By combining equations (5) and (6), the combined method may partly solve the problem because α_i is calculated for each dike, from the measurements of λ and α_f (Table 2 and Figure 7c). Given values of λ and α_f theoretically provide two solutions for α_{ic}, one smaller and the other larger than 90° (Figure 2c). A value of $\alpha_i > 90°$ would imply folding of the dikes. However, folds are never observed on site C1, thus only $\alpha_{ic} \leq 90°$ are considered. In a second step, γ_c is calculated from α_{ic} and λ using equation (5) (Table 2 and Figure 7d), or from α_{ic} and α_f using equation (6). The advantage of this method is that we take into account both the heterogeneous stretching (as in the stretching method) and the homogeneous deformation (as in the angle method) of the dikes.

[38] The calculated α_{ic} range from 12 to 64°. The less deformed dike D1 gives α_{ic} of 28.5° from a λ of 1.2 and a α_f of 26°. This results yield to a γ_c of 0.2, which is identical to γ_S. For the very deformed dikes D7 and D15, α_f cannot be measured precisely but only assumed to be $\leq$5°; the resulting α_{ic} are thus maximum estimates (Figure 7). In contrast, underestimate of λ will minimize α_{ic} (Figure 7). With λ equal to 5.7 and 14.6 for D7 and D15, respectively, the values of α_{ic} are $\leq$12° and $\leq$19.5°, resulting in γ_c of 6.7 and 8.6. Both values are higher than γ_S but lower than the minimum γ_A ($\geq$9.7, Table 2). We also applied this method to the transposed dikes analyzed by *Lacassin et al.* [1993] and the estimated α_{ic} range between 18.5° and 49°, which provide γ_A between 5.5 and 10.5 (Table 2). The intermediate dike D18 has a relatively high λ = 8.4 for an average α_f = 18°; the corresponding α_{ic} is particularly high at 64° inducing a low γ_C = 2.6. This value is bounded by the values of γ_A and γ_S for D18. The intermediate dike D12 (entire dike) has a λ = 10.6 for an average α_f = 13.9° that yield to a high α_{ic} of 51.5° and the corresponding γ_C = 3.2. For the most deformed part of D12, α_{ic} calculated with $w_i = w_m$ is 30.8° and the corresponding γ_C is 4.9, similar to γ_S and γ_A. Considering $w_i = w_u$ yields to higher α_{ic} (64.5°) and γ_C (6.1). In general, the combined method provides γ_C estimates in between those from the stretching and angle methods.

3.4. Age of the Deformed Dikes

3.4.1. Analytical Methods

[39] Ten leucocratic dikes showing various degrees of deformation were selected and sampled with a portable saw (Figures 4 and 5). Individual samples weighed 5 to 10 kg, but only five dikes yielded enough monazites in order to be dated: D1 (samples YY15 and YY16), D12 (sample YY29), D18 (sample YY27 and YY28), D15 (YY22) and D7 (YY23 and YY24) (Figures 4 and 5). Monazites grains were separated using successively a Wilfey table, heavy liquids, and a Frantz magnetic barrier separator. Monazites grains were selected by handpicking and mounted in epoxy and polished down to expose circa equatorial sections. Final selection of monazites for dating was based on backscattered electron (BSE) images (Figure 8) allowed identification of inclusion as well as growth zones that possibly recorded different geological events. BSE investigations were carried out at the Electron Microscope Unit at the Australian National University with a Cambridge S360 scanning electron microscope using a voltage of 20 kV, a current of ~2 nA and a working distance of ~20 mm.

[40] Analyses for U, Th, and Pb were performed on the SHRIMP II ion microprobe at the Research School of Earth Sciences (RSES, Australian National University, Canberra). Data were acquired as described by *Williams et al.* [1996], using reduced primary beam and spot size in order to decrease the ThO ion emission. Energy filtering was applied to suppress the inference on ^{204}Pb [*Rubatto et al.*, 2001]. Monazite 44069 of age 424.9 ± 0.4 Ma [*Aleinikoff et al.*, 2006] was used as standard material. Fractionation between $^{232}ThO^+$ and $^{238}UO^+$ was corrected by a factor calculated using the correlation between $^{232}ThO^+/^{238}UO^+$ and radiogenic $^{208}Pb/^{206}Pb$ as described by *Williams et al.* [1996]. Isotopic ratios were corrected for common Pb according to the measure ^{204}Pb and adopting the lead composition of *Stacey and Kramers* [1975]. The $^{238}Pb/^{232}Th$ ages were preferred to $^{206}Pb/^{238}U$, in order to avoid the problem of excess ^{206}Pb reported in similar samples [*Schärer et al.*, 1990]. Age calculation was done using the software Isoplot/Ex. Isotopic ratios and single ages are reported with 1σ error, whereas mean ages are given at the 95% confidence level.

3.4.2. Dikes Ages

[41] The studied leucocratic dikes are coarse grained and consist mainly of quartz, K-feldspar, plagioclase, with minor biotite and muscovite. Th-Pb ion probe data are listed in Table 3 and plotted in Figure 9.

[42] Monazites from the less deformed dike (D1, sample YY15) show oscillatory zoning confirming their magmatic origin (Figure 8a). The $^{208}Pb/^{232}Th$ ages are relatively well grouped between 21.7 ± 0.5 Ma and 23.3 ± 0.4 Ma with the exception of two older ages at 24.9 ± 0.4 Ma and 25.8 ± 0.7 Ma. If these two older analyses are excluded, the average calculated age is 22.55 ± 0.25 Ma (MSWD 1.2, Figure 9). In this sample, the Th age is in agreement with a $^{206}Pb/^{238}U$ age of 22.60 ± 0.21 Ma (MSWD 1.0). For the other samples below, with the exception of YY22, $^{206}Pb/^{238}U$ ages are generally 5–8% older than $^{208}Pb/^{232}Th$ ages, suggesting the presence in the monazite of significant excess ^{206}Pb.

[43] Monazites from both intermediate dikes (D12, sample YY29, and D18, sample YY27) show a more complicated internal structure with patchy zoned cores and unzoned or oscillatory zoned rims (Figures 8b and 8c). In sample YY27, ages range continuously between 22.5 and 31.6 Ma, making it difficult to ascribe an emplacement age to D18. Assuming these ages represent monazites crystallization from a melt in the dike, the data would rather suggest a protracted history for the dike. This could be possible in a feeding dike with persistent presence of melt, and thus monazite crystallizing over a long period. In this case, the youngest monazite would constrain the final crystallization of the melt. Given this uncertainty on the crystallization age, D18 was not used for the strain rate calculations. In sample

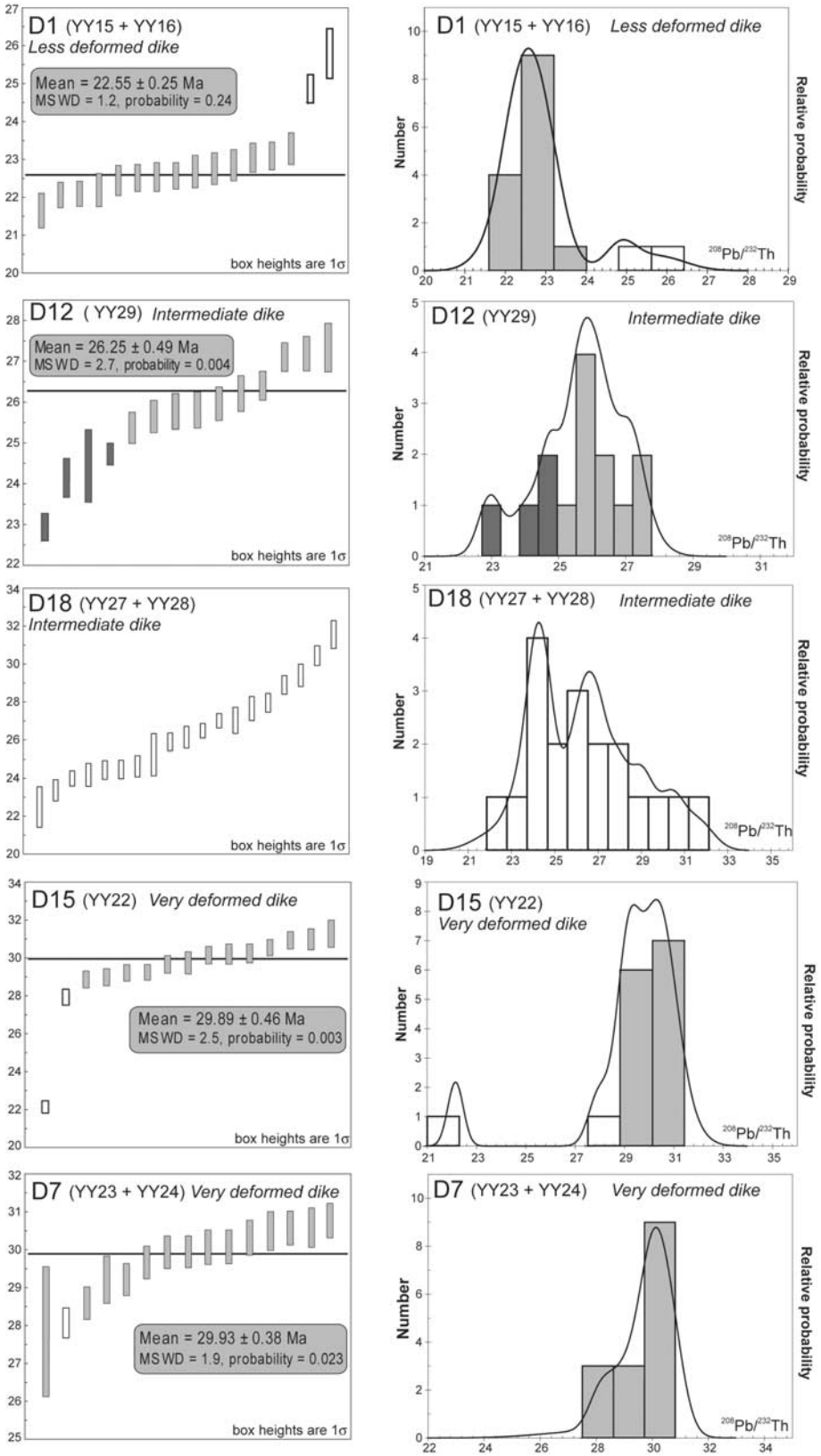

Figure 9. Graphs showing SHRIMP Th-Pb ages of monazites for each dike. Samples belonging to the same dike have been grouped. Plots were drawn with Isoplot software. (left) Individual $^{208}Pb/^{232}Th$ ages of monazites (1 sigma) as well as average ages (95% of confidence level) of data clusters. Analyses plotted in gray are used to calculate mean ages, whereas ages represented in white were excluded from the mean calculation. (right) Age histogram and relative probability plots. Geochronology results are summarized in Table 3.

Table 3. Monazite SHRIMP Th-Pb Data

Sample-Spot Name	Spot Location[a]	U (ppm)	Th (ppm)	$^{232}Th/^{238}U$	Percent of Common ^{206}Pb	$^{208}Pb/^{232}Th$	Percent Error	$^{208}Pb/^{232}Th$ Age (Ma)	1σ Error
D1 Less Deformed Dike (Samples YY15 and YY16)									
YY15-16		4278	86194	20.8	1.84	0.0011	2.1	21.7	0.5
YY15-10		4392	88443	20.8	0.00	0.0011	1.5	22.1	0.3
YY15-13		5303	88427	17.2	2.42	0.0011	1.5	22.1	0.3
YY15-3		4267	69732	16.9	3.84	0.0011	2.0	22.2	0.4
YY15-12		3023	60816	20.8	1.52	0.0011	1.8	22.5	0.4
YY15-5		6736	105963	16.3	2.58	0.0011	1.6	22.5	0.4
YY15-8		4004	66678	17.2	0.16	0.0011	1.7	22.5	0.4
YY15-14b		4520	74578	17.0	0.00	0.0011	1.6	22.6	0.4
YY15-6		5677	98011	17.8	1.36	0.0011	1.9	22.7	0.4
YY15-15		3545	72707	21.2	0.00	0.0011	1.8	22.8	0.4
YY15-7		3508	74304	21.9	2.16	0.0011	1.8	22.9	0.4
YY15-11		5714	110071	19.9	2.41	0.0011	1.7	23.1	0.4
YY15-4		5591	82203	15.2	0.66	0.0011	1.6	23.1	0.4
YY15-2		5627	95051	17.5	1.70	0.0012	1.8	23.3	0.4
YY15-9[b]		7978	83681	10.8	0.11	0.0012	1.5	24.9[b]	0.4
YY15.1[b]		4665	83022	18.4	3.35	0.0013	2.5	25.8[b]	0.7
D12 Intermediate Dike (Sample YY29)									
YY29-8[b]	core	6230	108323	18.0	1.39	0.0011	1.5	22.9[b]	0.3
YY29-9[b]	core	2485	129946	54.0	3.54	0.0012	2.0	24.1[b]	0.5
YY29-11[b]	core	721	54720	78.5	20.42	0.0012	3.7	24.4[b]	0.9
YY29-13[b]		4416	79230	18.5	1.37	0.0012	1.1	24.7[b]	0.3
YY29-5		6569	117159	18.4	0.98	0.0013	1.5	25.4	0.4
YY29-7	rim	4382	77753	18.3	1.92	0.0013	1.5	25.7	0.4
YY29-2	rim	5445	79956	15.2	3.33	0.0013	1.7	25.8	0.4
YY29-10	rim	2515	63075	25.9	3.02	0.0013	1.7	25.8	0.4
YY29-6	core	5836	103216	18.3	1.81	0.0013	1.6	26.0	0.4
YY29-1	core	5403	89890	17.2	0.61	0.0013	1.7	26.2	0.4
YY29-12	core	3412	60394	18.3	0.00	0.0013	1.3	26.4	0.4
YY29-9.1	rim	4047	62674	16.0	3.13	0.0013	1.3	27.1	0.4
YY29-4		3662	74704	21.1	0.17	0.0013	1.6	27.2	0.4
YY29-3	core	1878	50456	27.8	4.40	0.0014	2.2	27.3	0.6
18 Intermediate Dike (Samples YY27 and YY28)									
YY27-1.1	rim	3605	56397	16.2	6.01	0.0011	4.7	22.5	1.1
YY27-7	rim	4806	93281	20.1	1.32	0.0012	2.4	23.4	0.6
YY27-11	rim	3566	75332	21.8	1.81	0.0012	1.7	24.0	0.4
YY27-5		2776	56240	20.9	0.00	0.0012	2.5	24.2	0.6
YY27-15		2937	63859	22.5	3.40	0.0012	2.0	24.4	0.5
YY27-4b		3986	78650	20.4	0.00	0.0012	2.0	24.5	0.5
YY27-9		3737	58291	16.1	2.98	0.0012	2.3	24.6	0.6
YY27-1.2	core	4465	68149	15.8	0.00	0.0012	4.3	25.2	1.1
YY27-2.2	rim	3146	67943	22.3	0.00	0.0013	1.8	25.9	0.5
YY27-13		5929	87104	15.2	2.89	0.0013	2.2	26.2	0.6
YY27-10		5004	98095	20.3	0.00	0.0013	1.4	26.5	0.4
YY27-14		6799	81494	12.4	0.00	0.0013	1.4	27.0	0.4
YY27-6	core	8861	182847	21.3	0.29	0.0013	2.5	27.0	0.7
YY27-2.1	core	3595	55418	15.9	0.34	0.0014	2.3	27.7	0.6
YY27-8		2972	41832	14.5	0.00	0.0014	1.8	28.0	0.5
YY27-12	core	3833	51907	14.0	1.96	0.0014	1.7	28.9	0.5
YY27-4		6297	96772	15.9	5.12	0.0015	2.0	29.4	0.6
YY27-1		3272	35352	11.2	1.93	0.0015	1.7	30.4	0.5
YY27-3		2527	23041	9.4	0.00	0.0016	2.3	31.6	0.7
D15 Early Dike (Transposed in Foliation: Sample YY22)									
YY22-2[b]	rim	5897	101815	17.8	1.44	0.0011	1.4	22.2[b]	0.3
YY22-3[b]	rim	3041	79868	27.1	1.19	0.0014	1.5	27.9[b]	0.4
YY22-11		3913	57549	15.2	2.08	0.0014	1.6	28.9	0.5
YY22-9	rim	2819	47081	17.3	2.66	0.0014	1.6	29.0	0.5
YY22-12		4551	63669	14.5	2.20	0.0014	1.5	29.2	0.4
YY22-4	core	4073	93401	23.7	3.05	0.0014	1.4	29.2	0.4
YY22-1	core	3274	48072	15.2	3.18	0.0015	1.6	29.7	0.5
YY22-14	rim	4615	67468	15.1	0.02	0.0015	2.0	29.7	0.6
YY22-15		3906	48535	12.8	1.32	0.0015	1.5	30.2	0.5
YY22-13	core	2493	40272	16.7	1.06	0.0015	1.8	30.2	0.5
YY22-10	core	3526	54504	16.0	1.66	0.0015	1.6	30.2	0.5
YY22-7		4082	73880	18.7	0.92	0.0015	1.4	30.5	0.4
YY22-6	core	3723	68413	19.0	0.17	0.0015	1.5	30.9	0.5
YY22-8		3476	64520	19.2	0.00	0.0015	1.8	31.0	0.6
YY22-5	rim	2462	42624	17.9	0.00	0.0015	2.3	31.3	0.7

Table 3. (continued)

Sample-Spot Name	Spot Location[a]	U (ppm)	Th (ppm)	$^{232}Th/^{238}U$	Percent of Common ^{206}Pb	$^{208}Pb/^{232}Th$	Percent Error	$^{208}Pb/^{232}Th$ Age (Ma)	1σ Error
D7 Early Dike (Transposed in Foliation: Samples YY23 and YY24)									
Y24-14		3798	62152	16.9	2.94	0.0014	6.1	27.8	1.7
Y24-5[b]	rim	4484	76231	17.6	0.00	0.0014	1.4	28.1[b]	0.4
Y24-3	rim	4359	78315	18.6	3.02	0.0014	1.6	28.6	0.4
Y24-4	core	4757	78123	17.0	1.71	0.0015	2.1	29.2	0.6
Y24-1		4462	67524	15.6	1.64	0.0015	1.5	29.2	0.4
Y24-6		4769	80067	17.3	2.04	0.0015	1.5	29.7	0.4
Y24-9		5207	86465	17.2	1.00	0.0015	1.5	29.9	0.4
Y24-8	rim	5717	89968	16.3	1.76	0.0015	1.4	30.0	0.4
Y24-11		4953	66790	13.9	1.47	0.0015	1.5	30.1	0.5
Y24-2	core	4443	75570	17.6	2.59	0.0015	1.4	30.1	0.4
Y24-10		4440	81463	19.0	3.02	0.0015	1.5	30.3	0.5
Y24-8.1	core	3446	53979	16.2	0.00	0.0015	1.7	30.5	0.5
Y24-7		4651	72232	16.0	0.00	0.0015	1.5	30.6	0.5
Y24-13		4232	54464	13.3	2.22	0.0015	1.6	30.6	0.5
Y24-12		4980	83251	17.3	0.16	0.0015	1.5	30.8	0.5

[a]Spot location identifies cores and rims when possible. Rim and core only when two spots in one monazite from BSE images observations.
[b]Analysis excluded from average age calculation (see Figure 9).

YY29 age dispersion is somewhat limited and, ~24 Ma ages were rarely measured. We thus suggest an emplacement age of 26.25 ± 0.49 Ma (Figure 9) as best estimate. The dike may have experienced some degree of prolonged monazite crystallization and/or a limited overprint at ~24 Ma.

[44] The most deformed dikes D15 (sample YY22), and D7 (sample YY24) contain monazites with zoning varying from oscillatory (Figures 8d and 8e), particularly in YY24, to patchy and homogeneous, with however little evidence of a core-rim structure. As suggested by the zoning, monazite ages mainly fall into a single group with few analyses showing younger ages. The average age of the main peaks are within error in the two samples with 29.89 ± 0.46 Ma in sample YY22 ($^{206}Pb/^{238}U$ age of 30.16 ± 0.39 Ma) and 29.93 ± 0.38 Ma in sample YY24 (Figure 9). In these samples the ~30 Ma age is thus interpreted as crystallization age.

[45] The obtained crystallization ages correlate well with the amount of deformation observed for each dike: the most deformed dikes being the oldest (Figure 5) and the cross-cutting dike being the youngest.

[46] The dike ages span from 29.93 ± 0.38 Ma to 22.55 ± 0.25 Ma in good agreement with the timing of shearing inferred from other sources (34–17 Ma, [*Schärer et al.*, 1990; *Harrison et al.*, 1992; *Schärer et al.*, 1994; *Harrison et al.*, 1996; *Gilley et al.*, 2003]) and previous monazite ages (19–34 Ma) including that of YS11 (22.7 ± 0.3 Ma), which was sampled from a nearby outcrop [*Schärer et al.*, 1994]. All dikes measured by *Lacassin et al.* [1993] are transposed and strongly deformed and thus most probably predate D7 and D15. Their upper age limit cannot be constrained but they started to deform after the initiation of left-lateral shear at 34–35 Ma [*Schärer et al.*, 1994; *Gilley et al.*, 2003]. It is important to note that the younger and almost undeformed dike (D1, 22.5 ± 0.25 Ma) is significantly older than the end of left-lateral deformation that occurred at ~17 Ma [*Leloup et al.*, 2001b].

3.5. Strain Rate Calculations

[47] As stated above, the strain rate $\dot{\varepsilon}$ is the amount of deformation per time unit. In this study, the deformation has been measured with the shear strain. If the shear strain of each dike is plotted against its age ($\gamma = f(\text{time})$), $\dot{\varepsilon}$ will be given by the slope of the array joining two dikes (Figure 10). According to this definition, it is possible to attempt (1) an incremental strain rate, which is the slope of the straight line joining two successive dikes, and (2) an integrated strain rate, which is the slope between the least deformed dike D1 and an other dike (D12, D7 or D15); here D1 is assumed as a reference because it is nearly undeformed and thus should be close to the end of deformation. Alternatively, an average strain rate (3) can also be estimated using a linear regression considering all dikes. All strain rate values are given in Table 4 for each shear strain previously estimated (γ_s, γ_a and γ_c). Overall strain rates are minimum values because the shear strains are underestimated.

[48] 1. The incremental strain rate theoretically highlights the evolution of strain rate during the time of deformation with the changes in the slope of the arrays between the successive dikes. Considering γ_s values, it yields incremental strain rates of 3.9×10^{-14} s^{-1} between D12 and D1 and 9.6×10^{-15} s^{-1} between D15 and D12. The very deformed dike D7 shows a shear strain smaller than that of the intermediate dike D12. That strongly suggests that D7 shear strain is underestimated. The calculation of the incremental strain rate consequently yields a negative value and cannot be considered as valid. Thus, with the stretching shear strain (γ_S), D7 is not taken into account for the calculation of strain rates (incremental, integrated or global). Using γ_A values, the estimates of incremental strain rates are 1.7×10^{-14} s^{-1} between D12 and D1 and 6.4×10^{-14} s^{-1} between D15-D7 and D12. Finally, with the combined shear strain γ_C, the incremental strain rates are 2.6×10^{-14} s^{-1} between D12 and D1, 4.9×10^{-14} s^{-1} between D15 and D12, and 3×10^{-14} s^{-1} between D7 and D12. The values of incremental strain rates are in the order of 10^{-14} s^{-1}, with the exception of one smaller strain rates in the order of 9×10^{-15} s^{-1}.

[49] 2. The integrated strain rates are identical to the incremental strain rates between D12 and D1 for each shear strain considered. Considering γ_S, the integrated strain rate is of 2.4×10^{-14} s^{-1} between D15 and D1 and 3.9×10^{-14} s^{-1} between D12 and D1. Calculations of integrated strain rate

with γ_A yield to values of 4.1×10^{-14} s^{-1} between D15–D7 and D1 and 1.7×10^{-14} s^{-1} between D12 and D1. Finally, the integrated strain rates estimated with γ_C are 2.6×10^{-14} s^{-1} between D12 and D1, 3.7×10^{-14} s^{-1} between D15 and D1 and 2.8×10^{-14} s^{-1} between D7 and D1.

[50] 3. An average strain rate represents an average at the scale of the outcrop and for the time span between the oldest and youngest dikes. An average strain rate was calculated using each shear strain method. Here, the linear regression was anchored on the less deformed dike D1 that should indicate the end of deformation on the studied outcrop. The different strain rates estimated from γ_S, γ_A and γ_C are very close, and range from 3×10^{-14} s^{-1} to 4×10^{-14} s^{-1}. D7 was excluded from the linear regression calculated with γ_S, because its shear strain seems highly underestimated compared to the dike D15, which exhibits the same age and consequently should have been deformed identically.

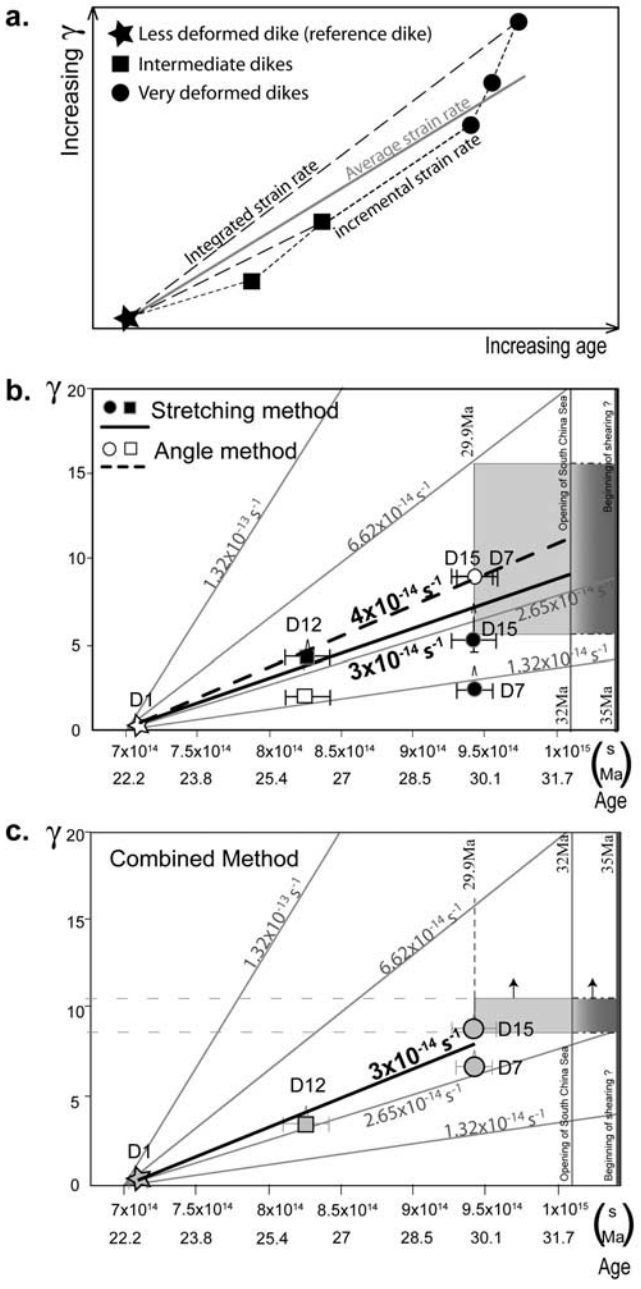

Figure 10. Diagrams of the evolution of shear strains through time and the calculation of the different strain rates. Shear strains are from Table 2 and Figure 7. Ages are from Table 3 and Figure 9. (a) Simplified graph showing different strain rates calculations: incremental (dot line), integrated (dashed line), and global (gray line). See text for details. (b) Shear strain results from stretching (black symbols) and angle (white symbols) methods. Horizontal error bars correspond to age uncertainties. Plots represent less deformed (star), intermediate (square), and very deformed dikes (circles). Arrows pointing up shows that shear strain are minimum estimates. Grey lines indicate average strain rates deduced from average fault rates for a 10, 20, 50, and 100 km wide shear zone. See text and Table 5 for details. Grey box corresponds to shear strain range measured by *Lacassin et al.* [1993] with the age expected from regional considerations. The upper time limit for left-lateral shear along the ASRR is set at 34–35 Ma [*Schärer et al.*, 1994; *Gilley et al.*, 2003]. Slope of linear regression anchored on D1 (bold black line) gives global strain. (c) Shear strain results from combined method. Legend is same as that for Figure 10b.

4. Discussion

4.1. Validity of Shear Strain Measurement

[51] In this study, all the methods used to estimate the shear strain are based on the assumption that deformation is close to simple shear. For the ASRRSZ, and particularly for the Ailao Shan massif, this assumption was thoroughly discussed by *Lacassin et al.* [1993]. These authors conclude that this assumption is most likely valid, because (1) the lineations are well defined and subhorizontal along the whole shear zone, (2) the YZ plan exhibits less stretched dikes than in the XZ plan, (3) shear criteria are all sinistral, and (4) there are no conjugate shear zones at outcrop scale. Furthermore, *Lacassin et al.* [1993] show that a strong flattening component on the order of 10% of pure shear for each simple shear increment is required to significantly alter the strain measurements. Such deformation would have induced a thinning by a factor 2 of the whole shear zone for a $\gamma = 10$, which is not observed. As the exhumation of the Ailao Shan mainly occurred during the left-lateral shear (see section 3.1), a distributed pure shear component may have induced the exhumation. However, at the site C1, the temperature was ~600°C at 22–23 Ma, and ~300°C at 22–21 Ma according to *Leloup et al.* [2001b]. These data reflect that the cooling was fast and started late in the shearing history of the Ailao Shan massif, i.e., after the emplacement of our younger dike. Thus, even though the exhumation was associated with a strong penetrative pure shear component, it would have occurred after the emplacement of the younger dike (D1) of age 22.55 ± 0.25 Ma. Thus, the assumption of simple shear deformation for that study is reasonable.

[52] In this regional NW–SE left-lateral shear regime, the orientation of the less deformed dikes is unexpected: they are perpendicular to the direction expected for tension gashes (i.e., parallel to σ_1 and perpendicular to σ_3). A first

Table 4. Strain Rate Calculations for the Incremental, Integrated, and Global Methods for γ_S, γ_A and γ_C

Way to Calculate Strain	Dikes Considered	Strain Rate (s^{-1})		
		γ_S	γ_A	γ_C
Incremental	D12-D1	3.9×10^{-14}	1.7×10^{-14}	2.6×10^{-14}
	D15-D12	9.6×10^{-15}	6.4×10^{-14}	4.7×10^{-14}
	D7-D12		6.4×10^{-14}	3.0×10^{-14}
Integrated	D12-D1	3.9×10^{-14}	1.7×10^{-14}	2.6×10^{-14}
	D15-D1	2.4×10^{-14}	4.1×10^{-14}	3.7×10^{-14}
	D7-D1		4.1×10^{-14}	2.8×10^{-14}
Average	All unless D7	3×10^{-14}	4×10^{-14}	3×10^{-14}

interpretation could be that the less deformed dikes have been emplaced after left-lateral shear ended, in another tectonic context, for instance NW–SE right-lateral shear. This is not the case because (1) other data show that left-lateral shear ended at ~17 Ma along the ASRR, more than 5 Ma after the emplacement of D1 (see section 3.1 and below) [*Harrison et al.*, 1996; *Leloup et al.*, 2001b], and (2) dike D12 shows an undeformed part with similar orientation to that of the less deformed dikes while the other part is strongly deformed according to a sinistral shear. A second possibility is that the less deformed dikes did emplace as tension gashes during left-lateral shear, thus with a SW–NE orientation, and were later rotated to their present position. This is highly improbable because such a deformation would induce a ~100% shortening resulting in folding of the dikes, followed by a ~200% stretching of the dikes. In the field, the dikes do not show any clear evidence of folding. A third hypothesis is that the dikes were emplaced in the same orientation as the less deformed dikes, i.e., perpendicular to the maximum principal stress. Indeed, in the ductile crust, the root zones of granites in strike-slip regime are expected to be parallel to the least principal stress [*Vigneresse*, 1995]. In our case, the orientations of the dikes are consistent with that of the least principal stress. Therefore, we consider the orientation of the least deformed dikes as the initial orientation of all dikes (i.e., $\alpha_i = 30°$).

[53] Because dike D12 presents an almost undeformed part (part a), it provides the opportunity to discuss some of the assumptions made in the stretching method. Measurements on the entire dike yield $e = 2.25$ and $\lambda = 10.6$, assuming that the initial width of the dike equals the present width of part a ($w_i = w_u$, Table 2). The same measurements limited to the most deformed part (part b) give $e = 5.04$ and $\lambda = 36.5$ assuming the same initial width ($w_i = w_u$). If, like for all other dikes, we assume that the initial width of the dike was equal to that of the widest boudin of part b ($w_i = w_m$), the results are different with $e = 2.42$ and $\lambda = 11.7$ (Table 2). This illustrates that the assumption on the initial width of dike in the stretching method may yield to largely underestimates of e and λ, which in turn lead to underestimate γ_S. In D12 case, γ_S appears underestimated almost by a factor 2 (5 versus 10.3).

[54] In contrast to the stretching method, the angle method avoids the problem of underestimating λ. However, γ_A is also underestimated for very deformed dikes that have a small final angle between the foliation and the deformed dike ($\alpha_f < 5°$). Therefore the angle method is mostly valid for relatively small deformation, where $\alpha_f > 5°$. Nevertheless for very deformed dikes, this method appears to give the least underestimates of γ (Table 2).

[55] In contrast with the two previous methods, the combined method avoids the assumption on the initial angle α_i by calculating it from λ and α_f. Nevertheless, it does not avoid the problem of λ underestimates, which result in underestimates of α_{ic} (Figure 7c), which in turn result in overestimates of γ_c (Figure 7d). Thus, the influence of λ underestimates appears to be limited. This is consistent with our data for very deformed dikes, for which γ_c are significantly larger than γ_s (Table 2), but not for intermediate dikes. For very deformed dikes, the accurate measurement of α_f is difficult, so that we consider $\alpha_f = 5°$, which is likely to overestimate the real angle. Thus, the calculated α_{ic} is overestimated (Figure 7c), resulting in underestimates of γ_c (Figure 7d).

[56] The three methods used in this study to estimate shear strains show some limitations. The stretching and angle methods require an assumption on α_i, whereas the combined method does not need it. The stretching and combined methods underestimate λ, whereas this problem is avoided with the angle method. However, the angle method provides minimum shear strains when the dikes are close to the foliation. In general, whatever the method used to estimate the shear strains, the results are all minimum values. The underestimate of shear strain is probably low for small deformation, but it might be larger for important deformation. That underestimate is hardly quantifiable, particularly when dikes do not exhibit any preserved segments. Thus, as no method seems more valuable than the others, all of them are used in the following section to calculate the strain rate.

4.2. Validity of Strain Rate Estimates

[57] As the strain rate is defined by the slope of the array joining two dikes, several ways were attempted to calculate the strain rates recorded by the dikes: incremental, integrated, and average strain rates (see section 3.5).

[58] For the incremental strain rates, the calculated values apparently exhibit some variations of strain rate between the different periods bounded by the ages of the dikes. However, the incremental strain rate is first sensitive to the chosen method of shear strain measurement. For instance, the incremental strain rate calculated with the stretching method seems to decrease during time, whereas it increases with the angle method and increases then decreases with the combined method. Another point of discussion is the small number of measurements and the scattering of the data. Only five dikes were dated and measured and the very deformed dikes exhibit different shear strains (see D15 and D7 with γ_c) although their ages are similar. Moreover, we cannot define any clear age for the emplacement of D18

Table 5. Strain Rates Calculated From the Fault Rates of the ASRRSZ Deduced From the Literature[a]

	Kinematic Constraints	Fault Rate (cm a^{-1})	Strain Rate (s^{-1})			
			For W = 10 km	For W = 20 km	For W = 50 km	For W = 100 km
Geological offsets[b]	maximum average rate	5.3	1.68×10^{-13}	8.40×10^{-14}	3.36×10^{-14}	1.68×10^{-14}
	minimum average rate	2.9	9.20×10^{-14}	4.60×10^{-14}	1.84×10^{-14}	9.20×10^{-15}
Zipper model		4.8	1.52×10^{-13}	7.61×10^{-14}	3.04×10^{-14}	1.52×10^{-14}
SCS sea floor spreading	average	3.7	1.17×10^{-13}	5.87×10^{-14}	2.35×10^{-14}	1.17×10^{-14}
Total average		4.2	1.32×10^{-13}	6.62×10^{-14}	2.65×10^{-14}	1.32×10^{-14}
SCS reconstruction with a proto-SCS	minimum offset (100 km)	0.5	1.59×10^{-14}	7.93×10^{-15}	3.17×10^{-15}	1.59×10^{-15}
	maximum offset (280 km)	1.4	4.44×10^{-14}	2.22×10^{-14}	8.88×10^{-15}	4.44×10^{-15}

[a]Geological offsets [*Leloup et al.*, 1993], Zipper model [*Harrison et al.*, 1996; *Leloup et al.*, 2001b], SCS seafloor spreading magnetic anomalies [*Briais et al.*, 1993; *Cande and Kent*, 1995], SCS reconstruction with a proto-SCS [*Clift et al.*, 2008] and for different shear zone width (W) equal to 10, 20, 50, and 100 km.

[b]Value of 700 ± 200 km between 34 and 17 Ma.

because the analyzed monazites revealed a complex crystallization story. Thus, the dike D7 was excluded to calculate the strain rates resulting from the stretching method, whereas the intermediate dike D18 was excluded for the whole strain rate measurements. For these reasons, the calculated incremental strain rates might not be representative and would require more precise strain estimates and/or more dikes to be analyzed.

[59] In the second case, the strain rate is integrated during the time span between the emplacement of each dike and that of D1, which is taken as reference. The fact that the time interval considered is longer than in the previous method reduces the influence of the age uncertainties on the resulting shear strain. However, the strain rate results are affected by any underestimate of the shear strain.

[60] The average strain rate corresponds to an average at the scale of the outcrop and for the considered period of time. Consequently, the average strain rate does not show the variations in strain rate during the time. However, when the data is limited, as it is in this case, the average strain rate is more representative than other estimates, because it reduces the effect of the scattering of data.

[61] We conclude that the most reliable method to estimate strain rates in this study is the average strain rate. However, we do not exclude that the incremental strain rate could be relevant in similar studies where the shear strains and ages of a larger number of dikes are measured.

4.3. Comparison With Other Strain Rate Data

[62] The strain rates measured in this study are in the range of expected natural strain rates (10^{-13} to 10^{-15} s^{-1}), according to *Pfiffner and Ramsay* [1982].

[63] The previous methods to measure direct strain rates were developed by using Rb-Sr dating of syntectonic fibrous strain fringes during successive deformation phases [*Müller et al.*, 2000], or by measuring $^{87}Sr/^{86}Sr$ ratios along transversal sections of helicitic garnets and the rotation of these garnets [*Christensen et al.*, 1989]. The method developed by *Müller et al.* [2000] shows strain rate variations from 1.1×10^{-15} s^{-1} to 7.7×10^{-15} s^{-1} recorded by ~5 mm pyrite crystals which rotated within slates in the hanging wall of a thrust, north to the North Pyrenean fault. The authors assigned the relatively low strain rate values to an underestimate of the strain, and to the sampling done outside the center of the shear zone. The method developed on helicitic garnet [*Christensen et al.*, 1989, 1994] estimated faster strain rates of 2.4×10^{-14} s^{-1} and $2.7^{+1.2}_{-0.7} \times 10^{-14}$ s^{-1} in the Appalachian and the Tauern window, respectively. These values measured at the mineral scale are close to our strain rate measurement of $\sim 3 \times 10^{-14}$ s^{-1} at the outcrop scale. Even though our strain rate value is probably underestimated, it is comparable to measurements made at much smaller scale but for similar durations (4 to 10 Ma). However, these direct strain rate estimates come from distinct deformation zones and cannot thus be compared further.

[64] Minimum shear strains, recalculated from previous elongation measurements of very deformed leucocratic dikes at site C1 (Figures 3 and 4, site 2 described by *Lacassin et al.* [1993]), are between 5.5 and 10.5 for γ_S, above 9.7 for γ_A, and between 8.6 and 10.3 for γ_C (Table 2). These dikes are among the most deformed of the outcrop and were too small to be sampled for dating. However, it is reasonable to think that these dikes are older than the comparatively less deformed D7 and D15. If we assume that these dikes are syntectonic, it implies that their ages range between ~35 Ma and 30 Ma. Their shear strains are plotted with that range of age in Figure 10 (gray box). The age range gives a rough constraint on the range of strain rate for these dikes, but the range of strain rate is compatible with our direct strain rate measurement of 3×10^{-14} s^{-1} (Figure 10). Conversely, the strain rate range estimated from the nondated dikes appear incompatible with shear strains lower than 1.4×10^{-14} s^{-1} for γ_S, 2.4×10^{-14} s^{-1} for γ_A, and 2.1×10^{-14} s^{-1} for γ_C.

[65] In the ASRRSZ, shear strains have also been estimated from amphibolitic boudins within mylonitic paragneisses, at a locality close to Mosha (site E1, Figure 3b) to the eastern boundary of the Ailao Shan massif (site 1 [*Lacassin et al.*, 1993]). These amphibolitic levels formed early in the metamorphism/strike-slip history of the shear zone and yield high shear strain of 33 ± 3 [*Lacassin et al.*, 1993]. That shear strain is twice higher than the shear strain estimated for the most deformed dikes at site C1. If the shear strain estimated with the amphibolitic boudins is reported to the total life span of the shear zone (34–17 Ma according to *Leloup et al.* [2001b]), it would imply a strain rate of 5.8×10^{-14} s^{-1}. However, the temperature dropped below 300°C at ~20 Ma at the site E1 according to *Leloup et al.* [2001b]. From that estimate, we may assume that the end of the ductile deformation occurred at ~20 Ma at the site E1, and thus reduced the time span for ductile deformation to about 14 Ma. Thus, the corresponding strain rate for a 14 Ma time span is $\sim 7 \times 10^{-14}$ s^{-1}, which is twice the average strain rate measured at site C1 (Figure 10). The difference between the strain rate values at site C1 and site

E1 could be explained by a strong underestimate of the shear strain at site C1 or by an important spatial heterogeneity of the deformation through the shear zone.

4.4. Implications on the Localization of Deformation

[66] The outcrop C1 shows clear evidence of heterogeneous deformation with the exceptional example of the intermediate dike D12: this dike shows a strongly deformed segment (part b) and an undeformed segment (part a) with respect to the surrounding rocks (Figures 4 and 5). Thus, such heterogeneous deformation may have occurred at the scale of the entire shear zone. Indeed, if the ductile deformation ended at ~22 Ma at site C1, it thus implies that deformation localized somewhere else until ~17 Ma, which is assumed to be the time of the end of left-lateral shearing along the ASRR [e.g., *Leloup et al.*, 2001b]. It is thus very likely that the fastest strain rates did not occur at site C1 but few kilometers to the east, where the heart of the shear zone may have been located prior to be crosscut by the active Red River normal fault [e.g., *Replumaz et al.*, 2001].

[67] Keeping in mind the last point, the direct strain rate value calculated in this study can be compared to the indirect strain rates estimated from fault rates and shear zone width only if we considered that the deformation was homogeneous within the total shear zone width.

[68] Along the ASRRSZ, with the extrusion model, the fault rate was estimated from three independent ways between 2.9 and 5.3 cm a^{-1} with an average of 4.2 cm a^{-1} (see section 3.1). The equivalent strain rates for a 10 km wide shear zone range between 9.2×10^{-14} s^{-1} and 1.7×10^{-13} s^{-1} (average of 1.3×10^{-13} s^{-1}, Table 5). These strain rate values are significantly higher than the strain rate estimate obtained in this study (Figure 10). Considering wider shear zones (20 km, 50 km or 100 km), with the same fault rates, it would imply slower strain rates (Table 5 and Figure 10). In turn, considering the model of *Clift et al.* [2008], the offset estimates give strain rates lower than the previous estimates, but the strain rate deduced from a maximum offset (280 km) for a 10 km wide shear zone is close to our measured strain rate (3 to 4×10^{-14} s^{-1}). Thus, these estimates would rather imply that the offsets were absorbed in a very narrow shear zone (Table 5).

[69] Conversely, the calculation of the width of a homogenous shear zone from a strain rate of 3×10^{-14} s^{-1} and an average fault rate of 4.17 cm a^{-1} would be 44 km. However, 44 km would rather correspond to a larger width bound because the deformation rate at site C1 is underestimated and was probably low with respect to the surrounding rocks, as suggested by high-strain measurements at site E1 and the presence of ultamylonitic zones (see section 4.3) [*Leloup et al.*, 1995]. This is consistent with the maximum outcrop width of gneisses along the ASRRSZ that is 40 km where the DNCV and AS overlap (Figure 3b). However, in order to estimate a precise shear zone width with respect to the hypothesis of heterogeneous deformation suggested by the observations in this study, it would require a continuous measurement of shear strains across the whole shear zone, which is currently out of range. In any case, if deformation had been absorbed in a very wide shear zone, it would imply either slow strain rates (i.e., 1.32×10^{-14} s^{-1} for W = 100 km, Table 5), which is incompatible with the results of this study (Figures 10b and 10c), or the existence of wide undeformed zones that have never been observed. Our results appear thus more compatible with a regime of localized deformation in the middle continental crust accommodating several hundreds of kilometers of relative motion through a few tens of kilometer wide shear zone, rather than with a regime of continuous and largely distributed crustal flow.

5. Conclusions

[70] In this paper, we presented a new method to measure average strain rates at the outcrop scale of a ductile shear zone, from a set of syntectonic dikes. This method was developed in a well-constrained major ductile shear zone: the Ailao Shan–Red River shear zone.

[71] We use three methods to estimate the shear strain of each dike. The two first methods (stretching and angle methods) were based on the measurement of the elongation of the leucocratic boudins trails or the final angle. Both methods required an assumption on the initial orientation of dikes. In contrast, the third method (combined method) allowed to recalculate the initial angle for each dike from their elongations and final angles, and then deduced their shear strain with either the stretching method or the angle method. Resulting shear strains correspond to minimum shear strains and vary between 0.2 and 9.7 from the least deformed dike to the most deformed ones.

[72] The emplacement of dikes was dated by ^{232}Th-^{208}Pb analyses on monazites by SHRIMP ion microprobe. Three groups of ages were obtained at circa 22.5 Ma, 26 Ma and 30 Ma. These ages are consistent with the structural observations: the most deformed dike being the oldest and the least deformed dike being the youngest.

[73] Whatever the method used to estimate the shear strains accumulated by the dikes, the average strain rate at the outcrop scale ranges from 3×10^{-14} s^{-1} to 4×10^{-14} s^{-1}. As the shear strains are minimum values, the resulting strain rate is a lower bound. However, this strain rate value is consistent with previous indirect and direct estimates of geological strain rates in shear zones. On the basis of former independent strain rates estimates on the Ailao Shan–Red River shear zone, we believe that the underestimate of the measured strain rate is likely to be not more than a half. Our measurement combined with previous estimates of the ASRR fault rates imply that the relative displacement along the ASRRSZ occurred at midcrustal depth in a less than 44 km wide shear zone, which is compatible with crustal-scale localized deformation mode.

[74] **Acknowledgments.** Financial support for field work was provided by the DYETI program. Geochronology was funded by UMR 5570 and the Australian Research Council. C. Sassier's Ph.D. scholarship at Laboratoire des Sciences de la Terre was supported by the Ministère de l'Enseignement Supérieur et de la Recherche, France. The Electron Microscopy Unit at ANU is thanked for access to the SEM facilities. Constructive reviews by W. Müller, C. Morley, and W. P. Schellart (AE) are gratefully acknowledged.

References

Aleinikoff, J. N., W. S. Schenck, M. O. Plank, L. Srogi, C. M. Fanning, S. L. Kamo, and B. Howell (2006), Deciphering igneous and metamorphic events in high-grade rocks of the Wilmington Complex, Delaware: Morphology, cathodoluminescence and backscattered electron zoning, and

SHRIMP U-Pb geochronology of zircon and monazite, *Geol. Soc. Am. Bull.*, *118*, 39–64, doi:10.1130/B25659.1.

Allen, C. R., A. R. Gillespie, Y. Han, K. E. Sieh, B. Zhang, and C. Zhu (1984), Red River and associated faults, Yunnan province, China: Quaternary geology, slip rates, and seismic hazard, *Geol. Soc. Am. Bull.*, *95*, 686–700, doi:10.1130/0016-7606(1984)95<686:RRAAFY>2.0.CO;2.

Anczkiewicz, R., G. Viola, O. Mütener, M. F. Thirlwall, I. M. Villa, and N. Q. Quong (2007), Structure and shearing conditions in the DayNuiCon Voi massif: Implications for the evolution of the Red River shear zone in northern Vietnam, *Tectonics*, *26*, TC2002, doi:10.1029/2006TC001972.

Armijo, R., F. M. Meyer, A. Hubert, and A. Barka (1999), Westward propagation of the North Anatolian fault into the northern Aegean: Timing and kinematics, *Geology*, *27*(3), 267–270, doi:10.1130/0091-7613(1999)027<0267:WPOTNA>2.3.CO;2.

Biermeier, C., and K. Stüwe (2003), Strain rates from snowball garnet, *J. Metamorph. Geol.*, *21*(3), 253–268.

Briais, A., P. Patriat, and P. Tapponnier (1993), Updated interpretation of magnetic anomalies and seafloor spreading stages in the South China Sea, implications for the Tertiary tectonics of SE Asia, *J. Geophys. Res.*, *98*, 6299–6328, doi:10.1029/92JB02280.

Brun, J.-P. (1999), Narrow rifts versus wide rifts: Inferences for the mechanics of rifting from laboratory experiments, *Philos. Trans. R. Soc. London, Ser. A*, *357*, 695–712, doi:10.1098/rsta.1999.0349.

Bureau of Geology and Mineral Resources of Yunnan (1983), Geological map of Yunnan, Kunming, China.

Cande, S. C., and D. V. Kent (1995), Revised calibration of the geomagnetic polarity timescale for the Late Cretaceous and Cenozoic, *J. Geophys. Res.*, *100*, 6093–6095, doi:10.1029/94JB03098.

Catlos, E. J., C. S. Dubey, T. M. Harrison, and M. A. Edwards (2004), Late Miocene movement within the Himalayan Main Central Thrust shear zone, Sikkim, north–east India, *J. Metamorph. Geol.*, *22*, 207–226, doi:10.1111/j.1525-1314.2004.00509.x.

Cherniak, D. J., and E. B. Watson (2001), Pb diffusion in zircon, *Chem. Geol.*, *172*, 5–24, doi:10.1016/S0009-2541(00)00233-3.

Cherniak, D. J., E. B. Watson, M. Grove, and T. M. Harrison (2004), Pb diffusion in monazite: A combined RBS/SIMS study, *Geochim. Cosmochim. Acta*, *68*(4), 829–840, doi:10.1016/j.gca.2003.07.012.

Christensen, J. N., J. L. Rosenfeld, and D. J. DePaolo (1989), Rates of tectonometamorphic processes from Rubidium and Strontium isotopes in garnet, *Science*, *244*, 1465–1469.

Christensen, J. N., J. Selverstone, J. L. Rosenfeld, and D. J. DePaolo (1994), Correlation by Rb-Sr geochronology of garnet growth histories from different structural levels within the Tauern Window, Eastern Alps, *Contrib. Mineral. Petrol.*, *118*, 1–12, doi:10.1007/BF00310607.

Clift, P., and Z. Sun (2006), The sedimentary and tectonic evolution of the Yinggehai-Song Hong basin and the southern Hainan margin, South China Sea: Implications for Tibetan uplift and monsoon intensification, *J. Geophys. Res.*, *111*, B06405, doi:10.1029/2005JB004048.

Clift, P., G. H. Lee, N. A. Duc, U. Barckhausen, H. V. Long, and S. Zhen (2008), Seismic reflection evidence for a Dangerous Grounds miniplate: No extrusion origin for the South China Sea, *Tectonics*, *27*, TC3008, doi:10.1029/2007TC002216.

Copley, A., and D. McKenzie (2007), Models of crustal flow in the India-Asia collision zone, *Geophys. J. Int.*, *169*, 683–698, doi:10.1111/j.1365-246X.2007.03343.x.

Davy, P., and P. R. Cobbold (1988), Indentation tectonics in nature and experiment, 1. Experiments scaled for gravity, *Bull. Geol. Inst. Uppsala*, *14*, 129–141.

Davy, P., and P. R. Cobbold (1991), Experiments on shortening of a 4-layer model of the continental lithosphere, *Tectonophysics*, *188*, 1–25, doi:10.1016/0040-1951(91)90311-F.

Dunlap, W. J., G. Hirth, and C. Teyssier (1997), Thermomechanical evolution of a ductile duplex, *Tectonics*, *16*, 983–1000, doi:10.1029/97TC00614.

England, P., and D. McKenzie (1982), A thin viscous sheet model for continental deformation, *Geophys. J. R. Astron. Soc.*, *70*, 295–321.

England, P., and P. Molnar (1997), Active deformation of Asia: From kinematics to dynamics, *Science*, *278*, 647–650, doi:10.1126/science.278.5338.647.

Fry, N. (1979), Random point distributions and strain measurement in rocks, *Tectonophysics*, *60*, 89–105, doi:10.1016/0040-1951(79)90135-5.

Garnier, V., G. Giuliani, H. Maluski, D. Ohnenstetter, T. P. Trong, V. H. Quang, L. P. Van, T. V. Van, and D. Schwarz (2002), Ar-Ar ages in phlogopites from marble-hosted ruby deposits in northern Vietnam: Evidence for Cenozoic ruby formation, *Chem. Geol.*, *188*, 33–49, doi:10.1016/S0009-2541(02)00063-3.

Gilley, L. D., T. M. Harrison, P. H. Leloup, F. J. Ryerson, O. M. Lovera, and J.-H. Wang (2003), Direct dating of left-lateral deformation along the Red River shear zone, China and Vietnam, *J. Geophys. Res.*, *108*(B2), 2127, doi:10.1029/2001JB001726.

Gueydan, F., C. Mehl, and T. Parra (2005), Stress-strain rate history of a midcrustal shear zone and the onset of brittle deformation inferred from quartz recrystallized grain size, in *Deformation Mechanisms, Rheology and Tectonics: From Minerals to the Lithosphere*, edited by D. Gapais, J. P. Brun, and P. R. Cobbold, *Geol. Soc. London Spec. Publ.*, *243*, 127–142.

Hacker, B. R., A. Yin, J. M. Christie, and A. W. Snoke (1990), Differential stress, strain rate, and temperatures of mylonitization in the Ruby Mountains, Nevada: Implications for the rate and duration of uplift, *J. Geophys. Res.*, *95*, 8569–8580, doi:10.1029/JB095iB06p08569.

Hacker, B. R., A. Yin, J. M. Christie, and G. A. Davis (1992), Stress magnitude, strain rate, and rheology of extended middle continental crust inferred from quartz grain sizes in the Whipple mountains, California, *Tectonics*, *11*, 36–46, doi:10.1029/91TC01291.

Hall, R. (2002), Cenozoic geological and plate tectonic evolution of SE Asia and the SW Pacific; computer-based reconstructions, model and animations, *J. Asian Earth Sci.*, *20*, 353–431, doi:10.1016/S1367-9120(01)00069-4.

Handy, M. R., and J.-P. Brun (2004), Seismicity, structure and strength of the continental lithosphere, *Earth Planet. Sci. Lett.*, *223*, 427–441, doi:10.1016/j.epsl.2004.04.021.

Harrison, T. M., C. Wenji, P. H. Leloup, F. J. Ryerson, and P. Tapponnier (1992), An early Miocene transition in deformation regime within the Red River Fault Zone, Yunnan, And its significance for Indo-Asian tectonics, *J. Geophys. Res.*, *97*, 7159–7182, doi:10.1029/92JB00109.

Harrison, T. M., K. D. McKeegan, and P. LeFort (1995), Detection of inherited monazite in the Manaslu leucogranite by $^{208}Pb/^{232}Th$ ion microprobe dating: Crystallization age and tectonic implications, *Earth Planet. Sci. Lett.*, *133*, 271–282, doi:10.1016/0012-821X(95)00091-P.

Harrison, T. M., P. H. Leloup, F. J. Ryerson, P. Tapponnier, R. Lacassin, and C. Wenji (1996), Diachronous initiation of transtension along the Ailao Shan-Red River shear zone, Yunnan and Vietnam, in *The Tectonic Evolution of Asia*, edited by A. Yin and T. M. Harrison, pp. 208–226, Cambridge Univ. Press, Cambridge, U.K.

Helmcke, D. (1985), The Permo-Triassic ''Paleotethys'' in mainland Southeast-Asia and adjacent parts of China, *Geol. Rundsch.*, *74*, 215–228, doi:10.1007/BF01824893.

Holloway, N. H. (1982), North Palawan block, Philippines, its relation to Asian mainland and role in the evolution of the South China Sea, *AAPG Bull.*, *66*, 1355–1383.

Houseman, G., and P. England (1993), Crustal thickening versus lateral expulsion in the Indian-Asian continental collision, *J. Geophys. Res.*, *98*(B7), 12,233–12,250, doi:10.1029/93JB00443.

Huang, T. K. (1960), Characteristics of the structure of China: Preliminary conclusions, *Sci. Sin.*, *9*, 507–524.

Hubert Ferrari, A., G. King, I. Manighetti, R. Armijo, B. Meyer, and P. Tapponnier (2003), Long-term elasticity in the continental lithosphere: Modelling the Aden ridge propagation and the Anatolian extrusion process, *Geophys. J. Int.*, *153*, 111–132, doi:10.1046/j.1365-246X.2003.01872.x.

Jolivet, L., O. Beyssac, B. Goffé, D. Avigad, C. Lepvrier, H. Maluski, and T. T. Thang (2001), Oligo-Miocene midcrustal subhorizontal shear zone in Indochina, *Tectonics*, *20*, 46–57, doi:10.1029/2000TC900021.

Lacassin, R., P. H. Leloup, and P. Tapponnier (1993), Bounds on strain in large Tertiary shear zones of SE Asia from boudinage restoration, *J. Struct. Geol.*, *15*, 677–692, doi:10.1016/0191-8141(93)90055-F.

Lee, J. K. W., I. S. Williams, and D. J. Ellis (1997), Pb, U and Th diffusion in natural zircon, *Nature*, *390*, 159–162, doi:10.1038/36554.

Leloup, P. H., and J. R. Kienast (1993), High-temperature metamorphism in a major strike-slip shear zone: The Ailao Shan-Red River, Peoples Republic of China, *Earth Planet. Sci. Lett.*, *118*, 213–234, doi:10.1016/0012-821X(93)90169-A.

Leloup, P. H., T. M. Harrison, F. J. Ryerson, C. Wenji, L. Qi, P. Tapponnier, and R. Lacassin (1993), Structural, petrological and thermal evolution of a Tertiary ductile strike-slip shear zone, Diacang Shan, Yunnan, *J. Geophys. Res.*, *98*, 6715–6743, doi:10.1029/92JB02791.

Leloup, P. H., R. Lacassin, P. Tapponnier, U. Schärer, Z. Dalai, L. Xiaohan, Z. Lianshang, J. Shaocheng, and P. T. Trinh (1995), The Ailao Shan–Red River shear zone (Yunnan, China), Tertiary transform boundary of Indochina, *Tectonophysics*, *251*, 3–84, doi:10.1016/0040-1951(95)00070-4.

Leloup, P. H., R. Lacassin, P. Tapponnier, and T. M. Harrison (2001a), Comment on ''Onset timing of left-lateral movement along the Ailao Shan–Red River shear zone: $^{40}Ar/^{39}Ar$ dating constraint from the Nam Dinh area, northeastern Vietnam'' by Wang et al., 2000, *J. Asian Earth Sci.*, *18*, 281–292, *J. Asian Earth Sci.*, *20*, 95–99, doi:10.1016/S1367-9120(01)00034-7.

Leloup, P. H., N. Arnaud, R. Lacassin, J. R. Kienast, T. M. Harrison, T. T. Phan Trong, A. Replumaz, and P. Tapponnier (2001b), New constraints on the structure, thermochronology, and timing of the Ailao Shan–Red River shear zone, SE Asia, *J. Geophys. Res.*, *106*, 6683–6732, doi:10.1029/2000JB900322.

Leloup, P. H., R. Lacassin, and P. Tapponnier (2007), Discussion on the role of the Red River shear zone, Yunnan and Vietnam, in the continental extrusion of SE Asia, *J. Geol. Soc.*, *164*, 1253–1260, doi:10.1144/0016-76492007-065.

Maluski, H., C. Lepvrier, L. Jolivet, A. Carter, D. Roques, O. Beyssac, T. T. Tang, N. D. Thang, and D. Avigad (2001), Ar-Ar and fission-track ages in the Song massif: Early Triassic and Cenozoic tectonics in northern Vietnam, *J. Asian Earth Sci.*, *19*, 233–248, doi:10.1016/S1367-9120(00)00038-9.

McDougall, I., and T. M. Harrison (1988), *Geochronology and Thermochronology by the $^{40}Ar/^{39}Ar$ Method*, 212 pp. pp., Oxford Univ. Press, New York.

Morley, C. K. (2002), A tectonic model for the Tertiary evolution of strike-slip faults and rift basins in SE Asia, *Tectonophysics*, *347*, 189–215, doi:10.1016/S0040-1951(02)00061-6.

Morley, C. K. (2007), Variations in late Cenozoic-Recent strike-slip and oblique-extensional geometries, within Indochina: The influence of pre-existing fabrics, *J. Struct. Geol.*, *29*, 36–58, doi:10.1016/j.jsg.2006.07.003.

Müller, W., D. Aerden, and A. N. Halliday (2000), Isotopic dating of strain fringe increments: Duration and rates of deformation in shear zones, *Science*, *288*, 2195–2198, doi:10.1126/science.288.5474.2195.

Nam, T. N., M. Toriumi, and T. Itaya (1998), P-T-t paths and post-metamorphic exhumation of the Day Nui Con Voi shear zone in Vietnam, *Tectonophysics*, *290*, 299–318, doi:10.1016/S0040-1951(98)00054-7.

Pfiffner, O., and J. G. Ramsay (1982), Constraints on geological strain rates: Arguments from finite strain rates of naturally deformed rocks, *J. Geophys. Res.*, *87*, 311–321, doi:10.1029/JB087iB01p00311.

Ramsay, J. G. (1967), *Folding and Fracturing of Rocks*1967, 568 pp., McGraw-Hill, New York.

Ramsay, J. G. (2000), A strained Earth, past and present, *Science*, *288*, 2139–2141.

Ramsay, J. G., and M. I. Huber (1983), *The Techniques of Modern Structural Geology*, vol. 1, *Strain Analysis*, Academic, London.

Rangin, C., M. Klein, D. Roques, X. Le Pichon, and L. V. Trong (1995), The Red River fault system in the Tonkin Gulf, Vietnam, *Tectonophysics*, *243*, 209–222, doi:10.1016/0040-1951(94)00207-P.

Rangin, C., W. Spakman, M. Pubellier, and H. Bijwaard (1999), Tomographic and geological constraints on subduction along the eastern Sundaland continental margin (South–East Asia), *Bull. Soc. Geol. Fr.*, *170*, 775–788.

Replumaz, A., and P. Tapponnier (2003), Reconstruction of the deformed collision zone between India and Asia by backward motion of lithospheric blocks, *J. Geophys. Res.*, *108*(B6), 2285, doi:10.1029/2001JB000661.

Replumaz, A., R. Lacassin, P. Tapponnier, and P. H. Leloup (2001), Large river offsets and Plio-Quaternary dextral slip rate on the Red River fault (Yunnan, China), *J. Geophys. Res.*, *106*, 819–836, doi:10.1029/2000JB900135.

Rubatto, D., I. S. Williams, and I. S. Buick (2001), Zircon and monazite response to prograde metamorphism in the Reynolds Range, central Australia, *Contrib. Mineral. Petrol.*, *140*, 458–468, doi:10.1007/PL00007673.

Schärer, U. (1984), The effect of initial ^{230}Th disequilibrium on young U-Pb ages: The Malaku case, Himalaya, *Earth Planet. Sci. Lett.*, *67*, 191–204, doi:10.1016/0012-821X (84)90114-6.

Schärer, U., P. Tapponnier, R. Lacassin, P. H. Leloup, Z. Dalai, and J. Shaocheng (1990), Intraplate tectonics in Asia: A precise age for large-scale Miocene movement along the Ailao Shan–Red River shear zone, China, *Earth Planet. Sci. Lett.*, *97*, 65–77, doi:10.1016/0012-821X (90)90099-J.

Schärer, U., L.-S. Zhang, and P. Tapponnier (1994), Duration of strike-slip movements in large shear zones: The Red River belt, China, *Earth Planet. Sci. Lett.*, *126*, 379–397, doi:10.1016/0012-821X (94)90119-8.

Schellart, W. P., and G. S. Lister (2005), The role of the East Asian active margin in widespread extensional and strike-slip deformation in East Asia, *J. Geol. Soc.*, *162*, 959–972, doi:10.1144/0016-764904-112.

Schoenbohm, L. M., K. X. Whipple, B. C. Burchfiel, and L. Chen (2004), Geomorphic constraints on surface uplift, exhumation and plateau growth in the Red River region, Yunnan Province, China, *Geol. Soc. Am. Bull.*, *116*(7), 895–909, doi:10.1130/B25364.1.

Schoenbohm, L. M., B. C. Burchfiel, and C. Liangzhong (2006), Propagation of surface uplift, lower crustal flow and Cenozoic tectonics of the southeast margin of the Tibetan Plateau, *Geology*, *34*(10), 813–816, doi:10.1130/G22679.1.

Searle, M. P. (2006), Role of the Red River Shear zone, Yunnan and Vietnam, in the continental extrusion of SE Asia, *J. Geol. Soc.*, *163*, 1025–1036, doi:10.1144/0016-76492005-144.

Stacey, J. S., and J. D. Kramers (1975), Approximation of terrestrial lead isotope evolution by a two-stage model, *Earth Planet. Sci. Lett.*, *26*, 207–221, doi:10.1016/0012-821X(75)90088-6.

Stipp, M., H. Stünitz, R. Heilbronner, and S. M. Schmid (2002), Dynamic recrystallization of quartz: Correlation between natural and experimental conditions, in *Deformation Mechanisms, Rheology and Tectonics: Current Status and Future Perspectives*, edited by S. De Meer, M. R. Drury, J. H. P. De Bresser, and G. M. Pennock, *Geol. Soc. London Spec. Publ.*, *243*, 171–190.

Stöckhert, B., M. R. Brix, R. Kleinschrodt, A. J. Hurford, and R. Wirth (1999), Thermochronometry and microstructures of quartz-a comparison with experimental flow laws and predictions on the temperature of the brittle-plastic transition, *J. Struct. Geol.*, *21*, 351–369, doi:10.1016/S0191-8141(98)00114-X.

Tapponnier, P., and P. Molnar (1977), Active faulting and tectonics of China, *J. Geophys. Res.*, *82*, 2905–2930, doi:10.1029/JB082i020p02905.

Tapponnier, P., G. Peltzer, A. Y. Le Dain, R. Armijo, and P. R. Cobbold (1982), Propagating extrusion tectonics in Asia: New insights from simple experiments with plasticine, *Geology*, *10*, 611–616, doi:10.1130/0091-7613(1982)10<611:PETIAN>2.0.CO;2.

Tapponnier, P., G. Peltzer, and R. Armijo (1986), On the mechanics of the collision between India and Asia, in *Collision Tectonics*, edited by M. P. Coward and A. C. Ries, *Geol. Soc. Spec. Publ.*, *19*, 115–157.

Tapponnier, P., R. Lacassin, P. H. Leloup, U. Schärer, Z. Dalai, W. Haiwei, L. Xiaohan, J. Shaocheng, Z. Lianshang, and Z. Jiayou (1990), The Ailao Shan/Red River metamorphic belt: Tertiary left-lateral shear between Indochina and South China, *Nature*, *343*, 431–437, doi:10.1038/343431a0.

Taylor, B., and D. E. Hayes (1983), Origin and history of the south China Basin, in *The Tectonic and Geologic Evolution of Southeast Asian Seas and Islands, Part 2*, *Geophys. Monogr. Ser.*, vol. 27, edited by D. E. Hayes, pp. 23–56, AGU, Washington, D. C.

Vigneresse, J. L. (1995), Control of granite emplacement by regional deformation, *Tectonophysics*, *249*, 173–186, doi:10.1016/0040-1951(95)00004-7.

Wang, E., and B. C. Burchfiel (1997), Interpretation of Cenozoic tectonics in the right-lateral accommodation zone between the Ailao Shan shear zone and the eastern Himalayan syntaxis, *Int. Geol. Rev.*, *39*, 191–219.

Wang, E., B. C. Burchfiel, L. H. Royden, L. Chen, J. Chen, W. Li, and Z. Chen (Eds.) (1998a), *Late Cenozoic Xianshuihe-Xiaojiang, Red River, and Dali Fault Systems of Southwestern Sichuan and Central Yunnan, China*, *Spec. Pap. Geol. Soc. Am.*, *327*, 108 pp.

Wang, P. L., C. H. Lo, T. Y. Lee, S. L. Chung, C. Y. Lan, and N. Trong Yem (1998b), Thermochronological evidence for the movement of the Ailao Shan-Red River shear zone: A perspective from Vietnam, *Geology*, *26*(10), 887–890, doi:10.1130/0091-7613(1998)026<0887:TEFTMO>2.3.CO;2.

Wang, P. L., C. H. Lo, S. L. Chung, T. Y. Lee, C. Y. Lan, and T. V. Thang (2000), Onset timing of left-lateral movement along the Ailao Shan–Red River shear zone: $^{40}Ar/^{39}Ar$ dating constraint from the Nam Dinh area, northeastern Vietnam, *J. Asian Earth Sci.*, *18*, 281–292, doi:10.1016/S1367-9120(99)00064-4.

Williams, I. S., I. S. Buick, and I. Cartwright (1996), An extended episode of early Mesoproterozoic metamorphic fluid flow in the Reynolds Range, central Australia, *J. Metamorph. Geol.*, *14*, 29–47, doi:10.1111/j.1525-1314.1996.00029.x.

Xypolias, P., and I. K. Koukouvelas (2001), Kinematic vorticity and strain rate patterns associated with ductile extrusion in the Chelmos Shear Zone (External Hellenides, Greece), *Tectonophysics*, *338*, 59–77, doi:10.1016/S0040-1951(01)00125-1.

Zhang, L.-S., and U. Schärer (1999), Age and origin of magmatism along the Cenozoic Red River shear belt China, *Contrib. Mineral. Petrol.*, *134*, 67–85, doi:10.1007/s004100050469.

Zhou, D., K. Ru, and H. Chen (1995), Kinematics of Cenozoic extension on the South China Sea continental margin and its implications for the tectonic evolution of the region, *Tectonophysics*, *251*, 161–177, doi:10.1016/0040-1951(95)00018-6.

O. Galland, Physics of Geological Processes, Universitetet i Oslo, Sem Selands vei 24, NO-0316 Oslo, Norway.

P. H. Leloup, Laboratoire des Sciences de la Terre, Université de Lyon, Ecole Normale Supérieure de Lyon, Université Claude Bernard Lyon 1, CNRS, Bâtiment Géode, 43 Boulevard du 11 Novembre 1918, F-69622 Villeurbanne CEDEX, France. (herve.leloup@univ-lyon1.fr)

D. Lin and Y. Yue, Institute of Tibetan Plateau Research, Chinese Academy of Sciences, 18 Shuangqing Road, Haidian District, Box 2871, 100085 Beijing, China.

D. Rubatto, Research School of Earth Sciences, Australian National University, Mills Road, Canberra 0200, Australia.

C. Sassier, Volcanic Basin Petroleum Research, Oslo Research Park, NO-0349 Oslo, Norway.